PRC 92/01
H1 06/92-226

Technical Proposal

to build

Silicon Tracking Detectors for H1

H1 Collaboration

participating institutes

Deutsches Elektronen Synchrotron, DESY, Hamburg, Germany

Institut für Hochenergiephysik DESY, Zeuthen, Germany

Paul Scherrer Institut, Villigen, Switzerland

Institut für Mittelenergiephysik der ETH, Zürich, Switzerland

Physikinstitut der Universität Zürich, Switzerland

June 23, 1992

This proposal is supported by:

H.J. Behrend, J. Bürger, L.Criegee, G. Franke, J. Meyer,
V.Schröder, P. Steffen, G.G. Winter, N. Wulff, W. Zimmermann
Deutsches Elektronen Synchrotron, DESY, Hamburg, Germany

A. Bischoff, U. Harder, H.Henschel, H. Kaufmann, M. Klein,
P. Kostka, W. Lange, H. Lippold, J. Meissner, Th. Naumann, M. Winde
Institut für Hochenergiephysik DESY, Zeuthen, Germany

K. Gabathuler, R. Horisberger
Paul Scherrer Institut, Villigen, Switzerland

M. Brogle, R. Eichler, C. Grab, D. Pitzl
Institut für Mittelenergiephysik der ETH, Zürich, Switzerland

S. Egli, S. Steiner, U. Straumann, P. Truöl
Physikinstitut der Universität Zürich, Switzerland

Contents

Chapter 1

Introduction

We propose to complement the tracking devices of the H1 experiment at the HERA *ep*-collider with high resolution position sensitive detectors close to the beam line in the central and backward region. These detectors will improve the physics potential of the H1 experiment in two fields, namely the study of heavy quarks and of deep inelastic scattering at low x.

At the time when H1 was proposed [2] upgrades close to the beam line were already envisaged by reserving space for further subdetectors. An expression of interest outlining the physics motivation and the general design of these detectors has been submitted to the DESY Physics Research Committee in spring 1991 [1]. This technical proposal discusses the physics program in more detail and presents the technical design.

Physics Motivation

The interest in heavy quark physics is twofold: the tagging of heavy quark events in order to study the gluon structure function and the spectroscopy of charmed particles in rare and suppressed decay modes. Identification of heavy quark decays requires the separation of primary and secondary vertices of an event. This calls for a high resolution position sensitive detector situated as close to the interaction point as possible. Hence a new beam pipe with a reduced diameter is proposed.

The interest in low x physics is motivated by many open questions in the theoretical description of quark-gluon interactions at high parton densities. To explore the region of x down to $5 \cdot 10^{-5}$ it is mandatory to measure the scattered electron at small angles and energies. This again calls for detectors with high spatial resolution around a narrow beam pipe.

Silicon Detectors at Collider Experiments

Silicon strip detectors are well adapted to the physics needs outlined as they provide spatial resolutions of $10\,\mu$m with a minimum of occupied detector volume. Silicon strip detectors have been introduced in high energy physics experiments at an increasing rate during the last decade. At colliding beam machines, MARK II at the SLC was the first experiment to use a barrel shaped silicon strip detector for high precision vertex reconstruction [3]. DELPHI, ALEPH and OPAL at LEP are operating silicon vertex detectors and have produced first physics results. Recently, the CDF collaboration at the Fermilab $\bar{p}p$-collider installed a silicon vertex detector [4], which operates in an environement comparable to that at HERA.

The particular challenges for a silicon tracker at HERA are the following:

- the readout has to be matched to the bunch repetition rate of 10.4 MHz, requiring a multievent pipeline buffer,
- the length of the vertex detector has to be matched to the length of the luminous region,
- a support structure of low mass has to be designed in order not to deteriorate the performance of the existing tracking detectors in the forward and central region,
- a fast trigger which uses information from the silicon tracker has to be provided for electrons at small angles,
- the shielding of the central detector area against synchrotron radiation has to be improved and the front-end electronics has to be sufficiently radiation resistant.

All issues are addressed in this proposal.

General Outline of the Detector

The silicon detectors are located inside the innermost chamber of the H1 central tracking detector. The Central Silicon Tracker (CST) provides high resolution tracking and vertex reconstruction in the central region. The Backward Silicon Tracker (BST) measures particles at small angles with respect to the electron beam direction. A new beam pipe is proposed with an inner radius of 35 mm and a horizontal offset of 10 mm with respect to the beam line to allow for free transit of the direct synchrotron radiation.

The CST consists of two barrel shaped layers of double sided silicon strip detectors. The inner layer (radius $r = 40$ mm) is a regular prism with 10 faces, the outer one ($r = 75$ mm) with 16 faces. Each face consists of six silicon detectors (total length 360 mm) with readout at both ends. The CST is concentric with respect to the *beam pipe*.

The BST is composed of eight disks (four disks in the first stage) mounted perpendicularly to the beam line at distances between 280 mm and 860 mm from the nominal interaction point in the electron direction.

The disks have an inner hole of 55 mm radius and are segmented into 16 azimuthal sectors. The outer radius is 125 mm. In the final stage, each disk is built as a composite of three different silicon layers: one with pad segmentation for triggering, one with strips at constant radii (r-strips) to measure the polar angle of scattered electrons, and one layer with strips at constant azimuthal angles (φ-strips) to determine the transverse momentum of hadrons and electrons. The BST is concentric with respect to the *beam line*.

The 214 000 electronics channels are read out by a newly developed amplifier chip which contains a switched capacitor pipeline buffer and performs a multiplexed readout. A data reduction processor with hit finding and zero suppression and an interface to the H1 data acquisition system is being developed. The pad detectors require a special preamplifier which provides the input for the BST trigger.

Chapter 2

Physics and Design

2.1 Heavy Quark Physics with the Central Silicon Tracker

In electron-proton collisions heavy quarks are mainly produced through photon-gluon fusion. To a lower extent they originate from the hadronic content of the photon and intrinsic charm in the proton, see figure 2.1. The production cross section amounts to about 500 nb for charm

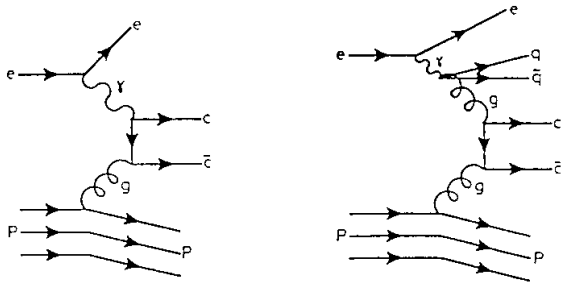

Figure 2.1: *Feynman diagrams for charm quark production via photon gluon fusion (left) and resolved photon (right).*

quarks and 5 nb for bottom quarks. With an anticipated integrated luminosity of $100\,\mathrm{pb}^{-1}$ per year, HERA will produce 10^8 charm/anticharm particles and 10^6 bottom/antibottom particles. The cross section is dominated by $Q^2 \sim 0$ and little transverse energy is visible in the detector. About 40% of the events are accepted by the H1 first level trigger.

Baryons and mesons containing c or b quarks have a decay length of the order of $100\,\mu\mathrm{m}$. A high resolution detector can resolve the event topology with primary and secondary vertices and discriminate against the more abundant background from events with light quarks.

Total Charm Cross Section and Gluon Structure Function

The total charm production cross section is sensitive to a variety of assumptions contained in the underlying QCD calculation. Higher order corrections (contained in the so-called K-factor) and the value of the charm quark mass [5] contribute most of the uncertainty of the cross section. Evaluated for the HERA kinematics, a cross section $\sigma(ep \rightarrow c\bar{c}X) = 0.68^{+0.26}_{-0.18}$ μb is predicted [6] for $m_c = 1.5\,\mathrm{GeV/c^2}$. A measurement of the cross section for an invariant mass of the $c\bar{c}$-pair close to threshold, where these corrections are most important, will reduce these uncertainties and determine m_c more precisely. The influence of different fragmentation schemes is comparatively small [8]. The transverse energy for production near threshold is small and therefore this region is suppressed by first level triggers. Consequently an improved charm tagging and discrimination against light quark pairs is particularly important.

Using the D^*-tagging technique we have shown [9, 10] that it is possible to reconstruct x_g, the momentum fraction of the proton carried by the gluon, and to extract the gluon structure function at low x_g ($0.001 \leq x_g \leq 0.1$). Present deep inelastic scattering experiments with μ- and ν_μ-beams and $Q^2 > 1\,\mathrm{GeV}^2$ probe the region $x_g > 0.01$ and the tagged photon spectrometer (Fermilab E691) [7] reaches $x_g > 0.04$.

$D^0 - \bar{D}^0$ Mixing and Doubly Cabibbo Suppressed Decays (DCSD)

The $D^0 - \bar{D}^0$ mixing predicted by the standard model is small compared to mixing in the K- and B-meson sector. The mass splitting Δm_D due to the box diagram is GIM-suppressed and the decay width $\Gamma_D \sim V_{cs}^2 \sim 1$ is large contrary to e.g. $\Gamma_B \sim V_{bc}^2 \sim (\sin\vartheta_c)^4$. Depending on the charm quark mass, the decay constant f_D, and the size of long distance effects, the mixing parameter

$$r_D = \frac{\text{Probability } (D^0 \rightarrow \bar{D}^0)}{\text{Probability } (D^0 \rightarrow D^0)} = \frac{1}{2}((\Delta m_D/\Gamma_D)^2 + (\Delta\Gamma/\Gamma_D)^2) \tag{2.1}$$

ranges between $5 \cdot 10^{-3}$ [11] and 10^{-4} [12]. Any larger mixing would signal new physics such as new vector particles, new scalars, horizontal symmetry or technicolour models. D^0-mesons at the time of production are identified by the charge of the accompanying low momentum pion in the decay $D^{*+} \rightarrow D^0\pi^+$ or $D^{*-} \rightarrow \bar{D}^0\pi^-$. Mixing is then recognized by the observation of wrong sign Kaons from $D^0 \rightarrow \bar{D}^0 \rightarrow K^+\pi^-, K^+\pi^-\pi^+\pi^-$. However, the same final state can be produced by doubly Cabibbo suppressed decays of D-mesons and the time evolution of the decay rate has to be measured to distinguish the two contributions.

The weak interaction eigenstates D_1 and D_2 are defined as a superposition of D^0 and $\bar{D}^0$ (neglecting direct CP violation)

$$D_1 = \frac{1}{\sqrt{2}}(D^0 + \bar{D}^0) \quad \text{and} \quad D_2 = \frac{1}{\sqrt{2}}(D^0 - \bar{D}^0) \tag{2.2}$$

and ρ denotes the complex ratio of wrong to right sign D-decay amplitudes,

$$\rho = \frac{\mathcal{A}(D^0 \rightarrow K^+\pi^-)}{\mathcal{A}(D^0 \rightarrow K^-\pi^+)} = \frac{\mathcal{A}(\bar{D}^0 \rightarrow K^-\pi^+)}{\mathcal{A}(\bar{D}^0 \rightarrow K^+\pi^-)}. \tag{2.3}$$

The decay rate $R(D^0 \rightarrow K^+\pi^-)$ at time t for a D^0 produced at time $t = 0$ is then

$$R(D^0 \rightarrow K^+\pi^-) = e^{-\Gamma t}\,\{\frac{1}{4}(x^2 + y^2)(\frac{t}{\tau})^2 + |\rho|^2 + (\frac{t}{\tau})[y\,\mathrm{Re}(\rho) + x\,\mathrm{Im}(\rho)]\}, \tag{2.4}$$

with the definitions

$$\Gamma = \Gamma_1 + \Gamma_2, \quad x = \Delta m/m, \quad \text{and } y = \Delta\Gamma/\Gamma \tag{2.5}$$

and τ is the D^0-lifetime. The measured time evolution allows to distinguish the mixing term (proportional $(\frac{t}{\tau})^2$) from the DCSD term (proportional $|\rho|^2$). Thus a high resolution vertex detector with a time resolution of $0.5 \cdot \tau$, corresponding to a vertex resolution of about $50\,\mu$m, is essential to separate mixing and DCSD. The sensitivity to the mixing parameter will be $5 \cdot 10^{-4}$, limited mainly by DCSD. The best experimental limit, $r_D \leq 4 \cdot 10^{-3}$ at 90 % C.L. was measured by the tagged photon experiment E691 [13].

The doubly Cabibbo suppressed decays are particularly interesting from the QCD-point of view and complete our understanding of weak meson decays. While singly suppressed decays, such as $D \to \pi\pi, K\bar{K}$ have been observed with branching ratios at the level of 10^{-3}, there exist only upper bounds at the same level for the doubly suppressed decays, with branching ratios expected of order 10^{-4}. Recently the E691 collaboration has published a first hint for a DCSD, namely $BR(D^+ \to \Phi K^+) = (4^{+2.2}_{-1.8} \pm 0.6) \cdot 10^{-4}$. With $100\,\text{pb}^{-1}$ the H1-detector will increase the world statistics by two orders of magnitude and, depending on background, find DCSD with branching ratios of a few times 10^{-5} to 10^{-6}.

Mode	Type	present limit (90% C.L.)	Experiment
$D^0 \to e^+e^-$	FCNC	$3.1 \cdot 10^{-5}$	E691
$D^0 \to \mu^+\mu^-$	FCNC	$1.1 \cdot 10^{-5}$	E615
$D^0 \to \mu^+e^-$	FCNC + LFV	$4.1 \cdot 10^{-5}$	E691
$D^+ \to \pi^+e^+e^-$	FCNC	$5.0 \cdot 10^{-4}$	E691
$D^+ \to \pi^+\mu^+\mu^-$	FCNC	$1.3 \cdot 10^{-4}$	E691
$D^+ \to \pi^+\mu^+e^-$	FCNC + LFV	$2.6 \cdot 10^{-4}$	E691
$D^0 \to K^0e^+e^-$	FCNC	$1.7 \cdot 10^{-3}$	Mark III
$D^0 \to \rho^0e^+e^-$	FCNC	$4.5 \cdot 10^{-4}$	CLEO
$D^0 \to \rho^0\mu^+\mu^-$	FCNC	$8.1 \cdot 10^{-4}$	CLEO
$c \to e^+e^-X$	FCNC	$2.2 \cdot 10^{-3}$	CLEO
$c \to \mu^+\mu^-X$	FCNC	$1.8 \cdot 10^{-2}$	CLEO

Table 2.1: *Upper limits on rare D decay branching ratios (90% C.L.).*

Flavour Changing Neutral Currents (FCNC)

In the standard model flavour changing neutral currents occur at the loop level only. Their rates are small and are sensitive to new heavy particles and to new physics in general. The observation of decays which are forbidden to all orders in the standard model, such as lepton-number violating decays (LFV), is a clear signal for new physics like technicolour, compositeness, leptoquarks or massive neutrinos. The present limits are summarized in table 2.1. H1 will increase the statistical sensitivity by at least one to two orders of magnitude with the proposed vertex detector and with $100\,\text{pb}^{-1}$. An important point in background rejection is muon and electron identification. For the lepton identification a lower momentum cut-off of $p_e \geq 1.0\,\text{GeV/c}$ and $p_\mu \geq 1.5\,\text{GeV/c}$ has been assumed. In ref. [14] we have shown by Monte Carlo simulation, that with an integrated luminosity of $10\,\text{pb}^{-1}$, which corresponds to the twentyfold statistics of the E691 experiment, the decays $D \to \mu\mu, ee$ can be observed with negligible background in the H1 detector.

Charmed Baryons

The charmed baryons Λ_c, Ξ_c^0, Ξ_c^+ and Ω_c can only decay weakly and therefore have observable decay lengths in a vertex detector. The cross section of baryon production is about 10% of the meson production and we can anticipate a substantial improvement of the world statistics in these weakly decaying charmed baryons. Theoretical predictions of branching ratios are more reliable in baryon decays than in meson decays because of the lower SU(3)-breaking and final state interaction effects [15]. Furthermore, the W-exchange diagrams can contribute without helicity suppression. However, non-perturbative corrections might be large. Table 2.2 summarizes the present knowledge relevant for H1 and indicates the quantities which could be measured with the proposed vertex detector. We note, that the spin 1/2 assignment for the Λ_c is not established yet.

Particle	Collaboration	decay mode	Events	measured quantities
Λ_c	ACCMOR	$pK3\pi, pK\pi, pK^0 2\pi, \Sigma\pi\pi, p\Phi$	$\sim$ 160	m; σ·B; $\frac{d^2\sigma}{dx_p dp_t^2}$, τ, pol.
	ARGUS	$pK^-\pi^+, \Lambda\pi^+\pi^-\pi^+, p\bar{K}^0, \Lambda\pi$	600	m; σ·B; $s \cdot \frac{d\sigma}{dx_p}$, pol.
		Λ e ν, $\Lambda\mu\nu$	73,30	σ·B
	CLEO	$pK\pi, \Lambda 3\pi, p\bar{K}^0, \Lambda\pi, \Xi Kp$	$\sim$ 500	B ; N(Λ_c)/N(D^0), pol.
	MarkI,II	$pK^-\pi^+$	40	m
	NA14/2	$pK^-\pi^+$	29	m; τ;N(Λ_c)/N(D^0)
	BIS-2	$\bar{K}^0 p\pi^+\pi^-$	130	m; σ·B;$E\frac{d^3\sigma}{dp^3}$
	E687	$pK^-\pi^+$	90	τ
Ξ_c^0	WA62,E687	$\Xi^-\pi^+$		seen
	ARGUS	$\Xi^-\pi^+$	18	m ; σ·B
		$\Xi^-\pi^+\pi^-\pi^+$	36	m ; σ·B
		Λ e, $\Lambda\mu$	25,20	σ· B
	ACCMOR	pK^-K^+, pK^-K^*	4	m ; σ·B; τ
	CLEO	$\Omega K, \Xi\pi$	9,38	m; σ·B
Ξ_c^+	ARGUS	$\Xi^-\pi^+\pi^+$	30	m ; σ·B; $s \cdot \frac{d\sigma}{dx_p}$
	ACCMOR	$\Xi^-\pi^+\pi^+$	3	m ; σ·B; $s \cdot \frac{d\sigma}{dx_p}$
		$\Sigma^+K^-\pi^+$	3	m ; σ·B
	CLEO	$\Xi^-\pi^+\pi^+$		m ; σ·B
Ω_c	ARGUS	$\Xi^- K^0\pi^+$	seen	

Table 2.2: *Selection of data on weak decays of charmed baryons. H1 will increase the statistics by an order of magnitude with the proposed vertex detector.*

A comparison of the observed and predicted (Lund MC) production ratio Λ_c/D shows a discrepancy of a factor two to four. The discrepancy seems lower in e^+e^- collisions (ARGUS, CLEO) than in photoproduction (E691, NA14/2) experiments. A tenfold increase in statistics will help to understand the origin of the increased Λ_c production. In addition we expect, like in electron-positron collisions, the production of polarised baryons. The BIS-2 collaboration [16], ACCMOR collaboration (NA32) [17], CLEO [18] and ARGUS [19] indeed found an indication of a Λ_c-polarisation.

Charmed baryons can be reconstructed by exploiting the particular kinematics of their decays to ΛX and using the $\Lambda \to p\pi$ (68%) decay as a tag. Background rejection is improved further by proton identification using dE/dx in the central jet chamber. This argument holds for decay

chains such as $\Lambda_c \rightarrow \Lambda\pi, \Lambda\pi\pi$; $\Xi_c^+ \rightarrow \Xi^-\pi^+\pi^+$ with $\Xi^- \rightarrow \Lambda\pi$ (100 %); $\Xi_c^0 \rightarrow \Xi^-\pi^+$ or $\Xi_c^0 \rightarrow \Omega^- K^+$ with $\Omega^- \rightarrow \Lambda K^-$. Another method of tagging e.g. Λ_c decays is the combination of pK^* with $K^* \rightarrow K\pi$ (100%).

Trigger Rates

The expected trigger rate R for events containing charm quarks at the anticipated peak luminosity $\mathcal{L}$ of HERA is

$$R = \sigma(ep \rightarrow c\bar{c}X) \cdot \mathcal{L} \cdot \epsilon_{trigger} = 500\,\mathrm{nb} \cdot 1.5 \cdot 10^{31}\,\mathrm{cm}^{-2}\mathrm{s}^{-1} \cdot 0.4 = 3\,\mathrm{Hz} \qquad (2.6)$$

and an order of magnitude higher for light quark production. The fraction of triggered events that contain charm quarks is therefore one order of magnitude more favourable at HERA than at the photoproduction experiment E691 with [20]

$$\frac{\sigma(\gamma p \rightarrow c\bar{c}X) \cdot \epsilon_{trigger}}{\sigma(\gamma p \rightarrow total) \cdot \epsilon_{trigger}} = \frac{0.5\,\mu\mathrm{b} \cdot 0.7}{100\,\mu\mathrm{b} \cdot 0.35} = 0.01. \qquad (2.7)$$

The statistics of E691 is 0.5 pb^{-1} with 2000 reconstructed D-decays [20], and the two Fermilab experiments E791 and E687 expect about two and one order of magnitude more, respectively. The experiment E791 had no charm-trigger and uses offline filters on 50 terabytes of data with a ratio of charm to triggers of 10^{-4} [21]. The CERN experiment WA92 (Omega) anticipates 200 000 reconstructed charm decays, which is of a similar order of magnitude as our proposal.

Performance of the CST for Heavy Quark Decays

For this proposal we studied the performance of the vertex detector for the D^*-tagging of charm [22]. Figure 2.2 shows the distribution of $\Delta M = M(K\pi\pi) - M(K\pi)$ from the decay chain $D^{*+} \rightarrow D^0\pi^+$ and $D^0 \rightarrow K^-\pi^+$. A clear peak at the mass difference of M(D^*) - M(D^0) is seen. No particle identification has been used. The combinatorial background in figure 2.2a originates from events without charm and can therefore be suppressed by the requirement of a secondary vertex. Using the CST a fit to a single vertex was made and only those events kept, which were incompatible with such a hypothesis. The background reduction is almost complete as seen in figure 2.2b. Especially no events were found with the wrong charge combination $D^0 \rightarrow K^+\pi^-$ and we conclude that this background is less than 0.8%.

A study of doubly Cabibbo suppressed decays and of $D^0 - \bar{D}^0$ mixing requires a measurement of the rate of the 'wrong' charge combination in the decay $D^0 \rightarrow K^+\pi^-$ as a function of the decay time, see equation 2.4. A vertex resolution of $\sigma \approx \tau_{D^0}/2$ is therefore necessary. Figure 2.3 shows the simulated vertex resolution in units of the D^0-lifetime as a function of the radius of the first detector layer and we conclude that a beam pipe radius of 35 mm should be aimed at.

2.2 CST Design Parameters

The vertex resolution is determined by the intrinsic position resolution of the detector, the multiple scattering in the material in front of the first measured point, and by the distance between the vertex and the first detector layer. In order to reconstruct secondary vertices in 3 dimensions, the vertex detector has to measure space points with comparable resolutions in the φ- and z-directions. The CST uses two layers of double sided silicon detectors with strips parallel to the z-axis on the p-side (junction side) and perpendicular on the n-side (ohmic side).

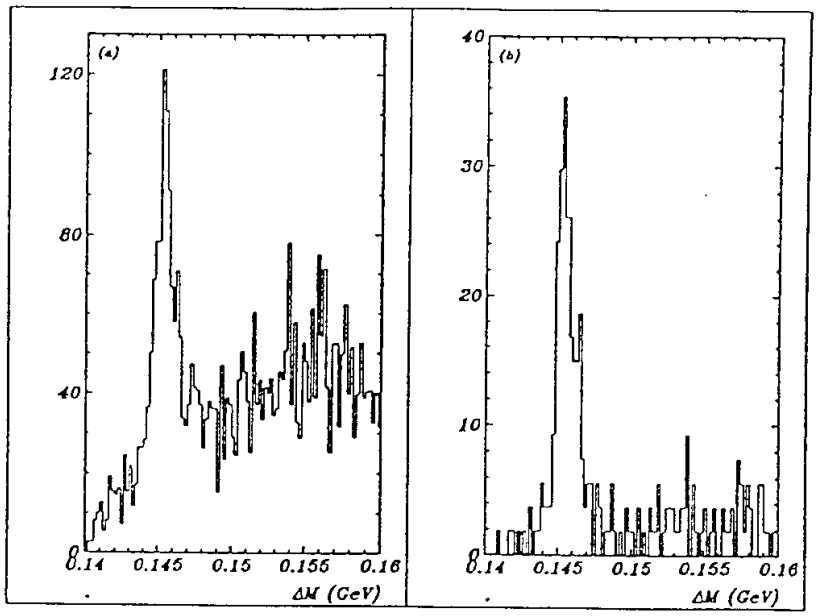

Figure 2.2: *Distribution of* $\Delta M = M(K\pi\pi) - M(K\pi)$ *before (a) and after (b) vertex constraint.*

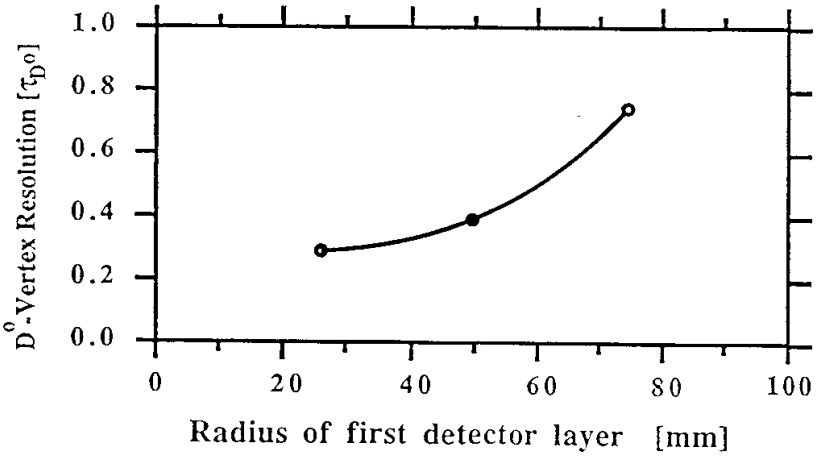

Figure 2.3: *Vertex resolution for the decay* $D^0 \to \mu\mu$ *in units of the* D^0*-lifetime* τ_{D^0} *versus the radius of the innermost layer of the detector. The increasing beam pipe wall thickness with radius is taken into account.*

Pattern recognition is performed in the central jet chamber and the z-chambers. Tracks are then linked to track elements found in the silicon vertex detector. The linking is uncritical due to the low local multiplicity expected for charm events at HERA. The momentum is measured from a combined fit using all tracking detectors. Primary and secondary vertices are reconstructed using a Kalman filter algorithm [23].

Beam Pipe Radius

The lower limit for the beam pipe radius is determined by machine requirements and background conditions. The injection procedure for the proton beam requires a minimal radius of 20 mm for the beam pipe in the interaction region. We decided to add a safety margin of 5 mm to this value. H1 already has a fixed synchrotron radiation mask which has a minimal distance of 25 mm from the beam axis. The second constraint at HERA is set by the synchrotron radiation. A series of dipole and off-axis quadrupole magnets placed between 24 m and 5.6 m from the interaction point deflects the electron beam by 10 mrad to achieve head-on collisions. The new beam pipe must not be hit by direct radiation, which is concentrated in the horizontal plane of HERA and displaced to the outside of the ring. With an upgrade of existing collimators, a beam pipe with a radius of 35 mm and a horizontal offset of 10 mm fulfills the constraints (details are given in chapter 3). The first detector layer has a radius of 40 mm and due to the horizontal offset the first measured point has a distance of 30 mm to the beam axis at the inside of the HERA ring, 40 mm in the vertical and 50 mm at the outside. The wall thickness for a carbon fibre beam pipe of 35 mm radius is 1.5 mm, corresponding to 0.6% of a radiation length.

Number of Layers

We propose a vertex detector with two layers in a barrel geometry (see figure 2.4). The efficiency of silicon strip detectors for minimum ionizing particles is about 97% due to Landau fluctuations and thresholds in hit-finding algorithms. Silicon strip detectors with very few defects can be produced with good yield. It is our aim to keep the fraction of dead channels in the full system below 2%.

The two layers of the CST are formed as regular prisms, with some overlap at the corners. Therefore, the geometric acceptance in azimuth is 100% of 2π. Along the z-direction, six wafers are placed in a row. Since the strips cannot extend to the wafer edge, an insensitive region of about 1 mm at each end, corresponding to 3% of the strip length, is unavoidable.

Adding inefficiencies and gaps, 85% of all tracks within the polar angle acceptance of the vertex detector are measured in both layers. About 18% of the tracks have a third hit in the overlap regions, which can be used in the alignment procedure. A third layer increases the fraction of 2-hit tracks to 98% and provide 3 hits for 78% of the tracks, but almost doubles the cost and the number of channels, since it has to be placed at a larger radius. It can be added at a later stage.

Detector Length

The length of the vertex detector has to be matched to the length of the luminous region at HERA. The proton bunch length is determined by the RF frequency of 208 MHz. The length of the electron bunches can be neglected in comparison. It is expected that 68% of the collisions occur in a region between $z = -90$ mm and $z = +90$ mm. Charm events with sufficient transverse

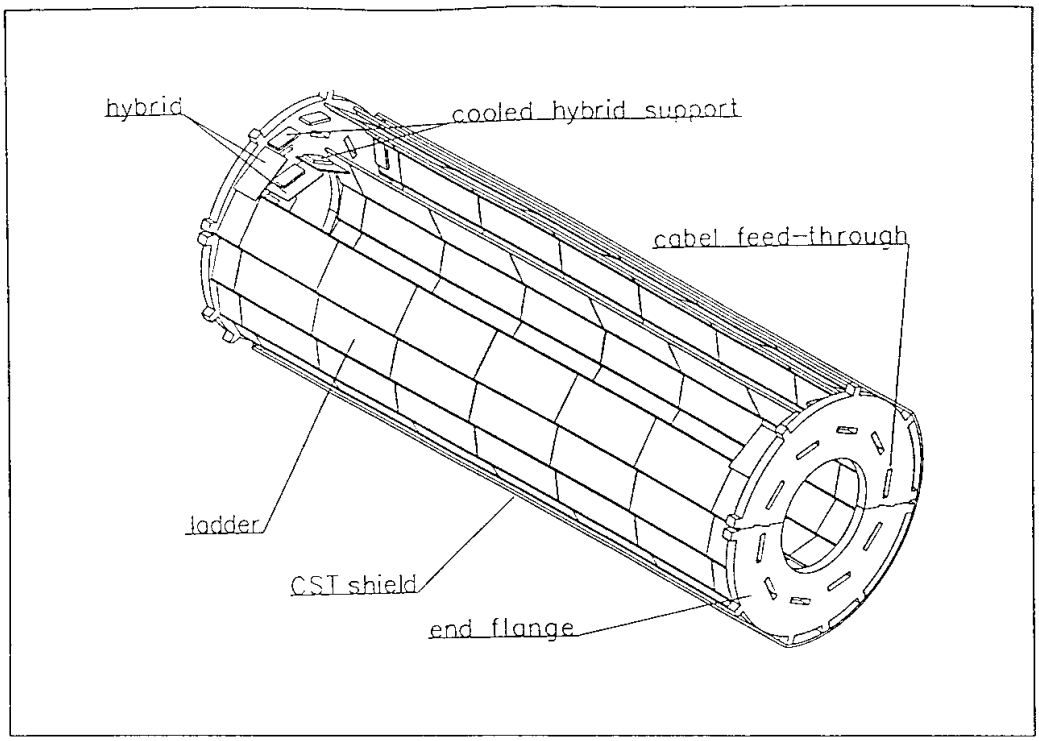

Figure 2.4: *Perspective view of the CST. The full length is 400 mm and the two silicon layers are placed at radii of 40 and 75 mm.*

momentum to fulfill the trigger requirements have an almost symmetric polar angle distribution. Therefore, the CST will be centered around the nominal interaction point in z.

The readout electronics are placed at the two end flanges, with only active silicon in between. The length of a single strip detector is limited to about 6 cm when 2 detectors are fabricated on a 4 inch wafer. Longer units can be formed by mounting two or three detectors in a row and daisy-chaining the strips with wire bonds. Such a unit is called a 'ladder' and includes a hybrid with the front-end electronics at one end. The total strip length is limited by the noise of the preamplifier which increases with the load capacitance. The prototype of our preamplifier achieves a signal-to-noise ratio of 15 : 1 for minimum ionizing particles with a load capacitance of 24 pF. The capacitance of one p-strip to its neighbours and to ground is about 1.2 pF/cm, which limits the total strip length to 20 cm. Our design uses ladders built from 3 detectors with a total length of 18 cm. Two ladders are joined mechanically to form a 'face' of 40 cm length (including the hybrids). Inner and outer layer of the CST are of equal length to simplify the mechanical construction. In the backward region, the inner layer provides an overlap with the first disks of the BST.

Fig 2.5a shows the geometric acceptance for particles from charm decays as a function of the full detector length. The acceptance is 40% for a length of 36 cm, while the solid angle coverage is 91%. The vertex resolution degrades for forward and backward tracks due to the increased distance to the first measured point and the longer path in scattering material. This is taken into account in Fig 2.5b by weighting each track with its impact parameter resolution. For a length of 36 cm, 65% of the maximum information is used.

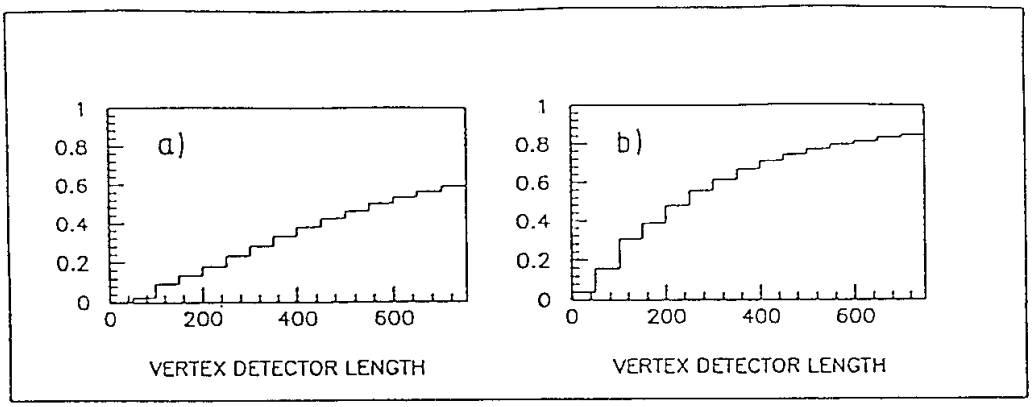

Figure 2.5: *a): Geometric acceptance of the CST for particles from D^0 decays versus the full detector length given in mm. The length of the HERA interaction region is taken into account. b): acceptance weighted by the impact parameter resolution of each track.*

Strip Pitch and Position Resolution

The front-end electronics is designed for a strip pitch of 50 μm. One detector is read out by 5 chips of 128 channels each, resulting in an active detector width of 32 mm. The same detector design is used for the inner and the outer layer. The inner layer has 10 faces at an average radius of 40 mm while the outer layer has 16 faces at an average radius of 75 mm. The overlap in φ is about 15% for the inner layer and 5% for the outer layer.

The intrinsic position resolution of silicon strip detectors depends on the strip pitch, the incident angle of the tracks and the signal-to-noise ratio of the electronics. The strip pitch on the p-side is 25 μm with every second strip being read out. The resulting position resolution in the $r-\varphi$ projection is 8 μm for tracks at normal incidence and 12 μm at 22° incidence, which occurs at the corners of the inner prism [24]. The magnetic field in H1 is 1.2 T, leading to a Lorentz angle of 4° for holes drifting in the silicon detectors. The resulting shift of the charge distribution collected on the p-strips is corrected by the reconstruction procedure.

The strips on the n-side are perpendicular to the strips on the p-side for measurement of the z-coordinate. The front-end electronics for the n-side is placed at the same detector edge as on the p-side, in order to simplify the mechanical construction and to avoid non-active material in the sensitive detector volume. A second metal layer on the n-side provides read out lines that route the signals along the detector to the amplifiers.

The interstrip capacitance on the n-side is 1.5–2.0 pF/cm. One strip has a length of 32 mm, so that 3 strips can be daisy-chained along a ladder. When three detectors are connected to form a ladder a threefold ambiguity arises for each hit. However, this ambiguity is on a scale of 6 cm and can be resolved easily. With 640 readout lines and a detector length of 58 mm, the pitch of the n-strips is fixed at 90 μm. The expected position resolution for the z-coordinate is 20 μm for tracks at normal incidence (0°), improving to 11 μm at 20° and becoming 32 μm at 60° [24]. Figure 2.6 shows the expected impact parameter resolution of the proposed silicon vertex detector for particles at $\vartheta = 90°$. At $p = 1$ GeV/c, a resolution of 60 μm is achieved.

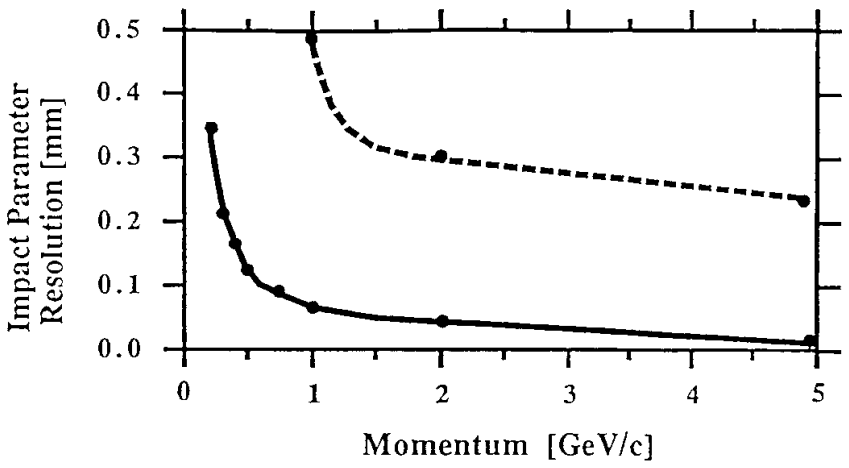

Figure 2.6: *Impact parameter resolution versus particle momentum for tracks at $\vartheta = 90°$. The dashed curve is for the present H1 detector, the solid curve includes the CST.*

2.3 Alignment of the CST

Experience at MARK II, DELPHI and ALEPH has shown that the ultimate alignment of a vertex detector is best done by software, using hits from the vertex detector itself and from outer tracking devices. The procedures used so far at LEP are rather complicated, in particular because one has to avoid systematic errors (on the micron level) induced by extrapolating tracks from outer tracking devices. Therefore it is desirable to employ a data-driven alignment method which uses hits from the vertex detector alone. For this purpose an alignment routine has been developed based on a vertex constraint technique that exclusively uses hits from a two layer vertex detector. The outer tracking devices are needed only for pattern recognition and momentum measurement.

The software alignment of the CST proceeds in two steps: First the individual wafers must be aligned relative to each other (internal alignment) and then the CST as a single rigid body must be aligned with respect to the rest of the H1 detector (global alignment). The second step, which is not really necessary for tasks where only CST data are required (e.g. looking for secondary vertices), is easy and not discussed here. The internal alignment, however, is the difficult part and has been studied quite extensively.

The concept of the alignment routine is to move and rotate all wafers simultaneously in space such that for each single-vertex event the tracks meet optimally in one space point (vertex constraint). Each wafer is assumed to be a flat and rigid silicon strip detector. Any possible bending or torsion of the wafers has to be measured before installation and is corrected for each hit. Since for each wafer there are six degrees of freedom (three translations and three rotations) the number of parameters to fit simultaneously the whole CST amounts to 936. To reduce this number to a more manageable level, the CST is subdivided into six rings along the beam axis, which are aligned individually. The interalignment of the rings relative to each other is then straightforward in one further iteration.

The problem is now reduced to a fit of 156 parameters (10·6 for the inner layer plus 16·6 for the outer layer). For each event the shortest distances $d_{i,k}$ between pairs of tracks (i, k) are calculated

as a function of the involved translation and rotation parameters, weighted and summed up (the tracks are assumed to be straight lines, for the effect of the magnetic field see below). The function to be minimized with respect to its 156 parameters is a sum over a number of events (NEV) with at least two tracks (NTR) in the ring:

$$\mathcal{F} = \frac{1}{2} \frac{\sum_{n=1}^{NEV} \sum_{\substack{i,k=1 \\ k>i}}^{NTR(n)} \frac{d_{i,k}^{2(n)}}{\sigma_i^{2(n)} + \sigma_k^{2(n)}}}{\sum_{n=1}^{NEV} NTR(n)[NTR(n)-1]} \quad . \tag{2.8}$$

The weights σ of each track are calculated by taking into account the intrinsic detector resolution and multiple scattering in the beam pipe and the silicon. A track passing through an overlap region is treated by replacing it by two independent tracks. The function $\mathcal{F}$ does not depend on the absolute position of the vertices in space and can be used for any arbitrary luminosity region and offset of the CST with respect to the beamline.

The effect of the magnetic field is included by replacing the helices with tangents calculated at the point of closest approach to a common event vertex. Thus new virtual hits are derived from the real hits and the procedure for straight tracks is applied.

The algorithm was tested using PYTHIA 5.6 to simulate one million light quark events via direct and resolved photon contributions. Among these were 20 000 events with at least two tracks in one ring having all a transverse momentum larger than 1.0 GeV/c. These events were tracked through the CST where all detectors were misaligned randomly between -0.1 mm and $+0.1$ mm for translations and between -1.5 mrad and $+1.5$ mrad for rotations (flat distributions). The function values before and after the alignment fit are $\mathcal{F} = 17.238$ and 1.141 respectively. A comparison with the function value for a perfectly aligned ring ($\mathcal{F} = 1.146$) shows that the fit routine is able to find the correct minimum. The value after the alignment fit is slightly lower because the alignment routine has reached a minimum which is influenced by a fluctuation due to the finite event sample used.

Assuming a 50% trigger efficiency for events from the electroproduction of two light quark jets, H1 will collect the event sample used above after an integrated luminosity of 4.3 pb^{-1}, 5.7 pb^{-1} and 14.7 pb^{-1} for the central, middle and outer rings, respectively. Raising the cut on the transverse momentum to 1.5 GeV/c (less multiple scattering and less influence of the magnetic field) increases the required integrated luminosity by a factor of five.

This alignment procedure is designed for events with a single vertex. However, it is not possible at H1 to have an event sample without a sizeable fraction of events with secondary vertices. Therefore we have also used an event sample with 50% admixture of $c\bar{c}$ events generated by PYTHIA. Results obtained so far show that such an admixture does not appreciably deteriorate the alignment quality.

2.4 Deep Inelastic Scattering with the Backward Silicon Tracker

When the H1 experiment was designed, a conservative beam-pipe design with a diameter of 190 mm was chosen which prevents the detection of electrons scattered backwards at large angles (according to the H1 convention the polar angle ϑ is defined with respect to the proton beam direction). Motivated by the strong recent emphasis on deep inelastic physics at low x we propose to implement a backward telescope consisting of silicon detector disks around a new narrow beam pipe. The extension of the kinematic range with the BST is illustrated in figure 2.7, showing lines of constant scattering angles and energies in the (Q^2, x) plane accessible at nominal HERA energies. The BST will allow to explore the region of very low x with a precision and lever arm in Q^2 superior to the presently installed detectors at HERA. This may lead to the discovery of recombination and saturation effects which would qualitatively change our understanding of quark and gluon interactions. Furthermore, the precise measurement of quark and gluon distributions at low x is important to calculate particle production rates at future high energy hadron colliders.

Figure 2.8 illustrates the acceptance of the BST for scattered electrons from a simulation of deep inelastic scattering events for $Q^2 \geq 4\ GeV^2$. Although the BST is fully efficient only in the angular region from 167° to 176°, it will detect more than 90% of the generated deep inelastic events above a Q^2 of 4 GeV^2 which corresponds to the lower acceptance edge of the BST. Note in particular that the BST has a high efficiency in the very low x region and also at large y.

Low x Physics

HERA will measure deep inelastic interactions down to $x \sim 5 \cdot 10^{-5}$ for the first time. At very small x the model of quasi-free, non-interacting partons [25] is no longer applicable because the predicted rise of structure functions at lower x conflicts with unitarity limits [27]. The standard linear QCD evolution equations [28] predict an increasing gluon distribution according to[1]:

$$\lim_{x \to 0} xG(x, Q^2) \sim \frac{\exp(z)}{\sqrt{2\pi z}} \tag{2.9}$$

where

$$z = \sqrt{2(\xi - \xi_0) C \ln \tfrac{1}{x}} \quad \text{and} \quad \xi = \ln \ln \tfrac{Q^2}{\Lambda^2}. \tag{2.10}$$

Another linear evolution equation, particularly adapted to describe the region of small x and moderate Q^2, has been derived by Fadin, Kuraev and Lipatov [30]. The rise of $xG(x, Q^2)$ at small x predicted by this evolution equation is even faster [31, 30]:

$$\lim_{x \to 0} xG(x, Q^2) \sim h(Q^2) x^{-1/2}. \tag{2.11}$$

Yet, the increase of the gluon density with decreasing x cannot continue infinitely as it leads to an unphysically large cross section violating unitarity. Therefore, at very small x the rise of the gluon density must be damped by a new mechanism. For high parton densities the gluons cannot be treated as free particles: recombination of gluon pairs competes with the parton decay processes considered in standard evolution equations. This effect, called 'screening', damps the fast increase of the gluon density.

The emerging qualitative picture for the evolution of the structure function $F_2(x, Q^2)$ at small x is illustrated in figure 2.9. Three regions A, B and C can be distinguished. Region A is described

[1] The subsequent discussion follows [29].

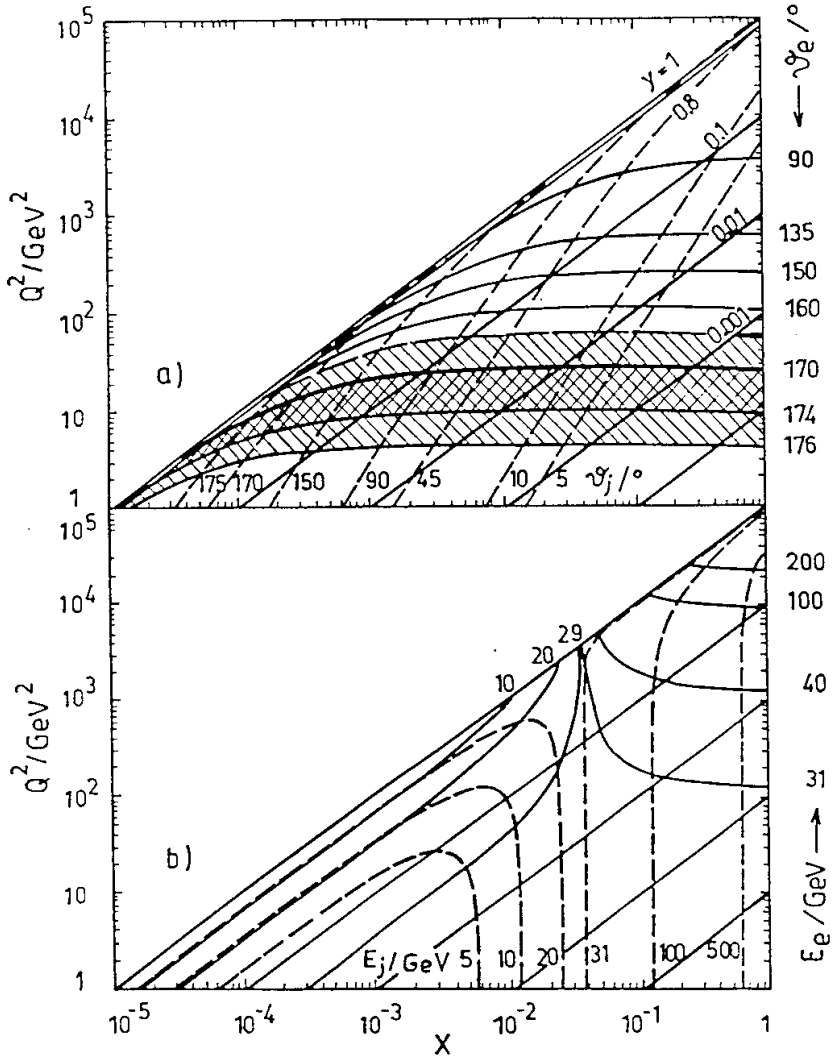

Figure 2.7: *Lines of constant scattering angles (a) and secondary energies (b) (solid: lepton (e,ν), dashed: jet) at HERA design energies 30 × 820 GeV². The angles are defined with respect to the proton beam direction. The dashed region shows the acceptance of the BST in phase 1 and 2. The central inner z-chamber covers angles up to* $\theta_e = 170°$.

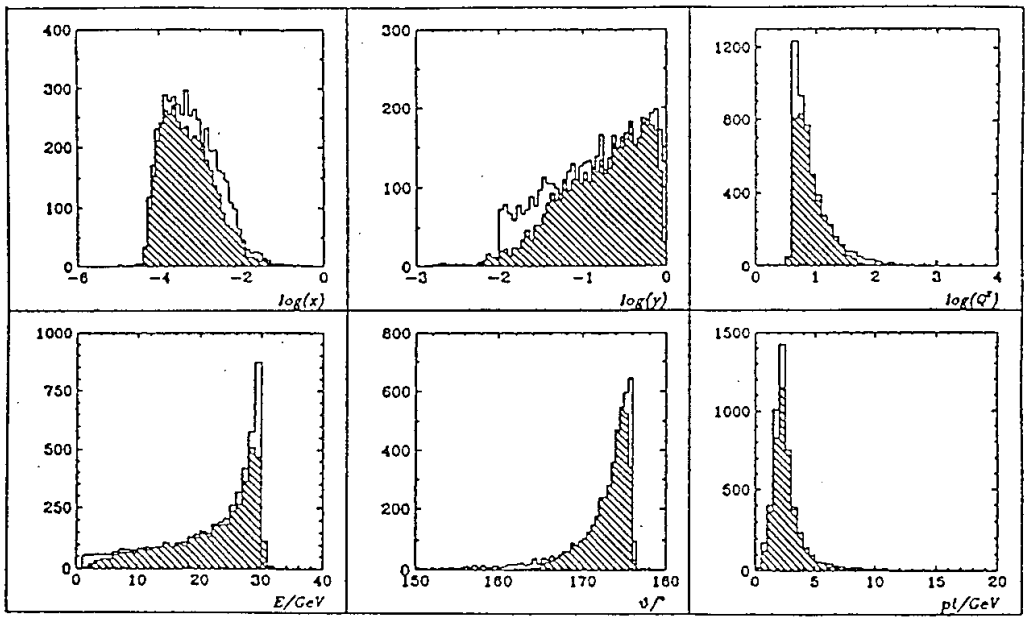

Figure 2.8: *Kinematical distributions of deep inelastic events generated according to cross section (MTB2) for* $Q^2 \geq 4\,GeV^2$ *and* $y \geq 0.01$. *The dashed histograms show the distributions of reconstructed scattered electrons traversing at least 3 planes of the BST (phase 2).*

by the standard leading-log QCD evolution equations, predicting an increase of $F_2(x, Q^2)$ with decreasing x. Region B is a transition region where recombination between gluons has to be taken into account, but the x evolution can be still described by improved evolution equations. Such evolution equations, which include non-linear terms, were first formulated in 1983 [27]. In region C the density of partons becomes so large that they cannot be considered free any longer and non-perturbative confinement effects will start to play a rôle. This region is the large Q^2 continuation of the Regge limit, for which we have no theoretical tool yet.

A quantitative prediction for the onset of regions B and C in the HERA kinematical domain depends on the assumptions made on the shape of the gluon distribution at some reference $Q_0^2 \sim 5\ GeV^2$ and especially on the 'strength' of the screening [32]. This strength is inversely proportional to the size of the region in the proton where the increase of the gluon density takes place. In case the growth of the gluon density is not spread uniformly in the proton, but smaller 'hot spot' regions are formed [33], the onset of deviations from the standard QCD evolutions will become visible earlier.

The unambiguous identification of the onset of a new regime from $F_2(x, Q^2)$ requires to reach the smallest possible values of x with high precision. A convenient way to quantify the necessary resolution is to study the derivative of F_2 with respect to $\ln Q^2$. Figure 2.10 illustrates a simulated measurement of $\partial F_2(x, Q^2)/\partial ln(Q^2)$ with the present H1 detector (shadowed region) and with the BST for $Q^2 \geq 5\,\mathrm{GeV}^2$. The points follow the parametrization B^- of [31] where the inner error

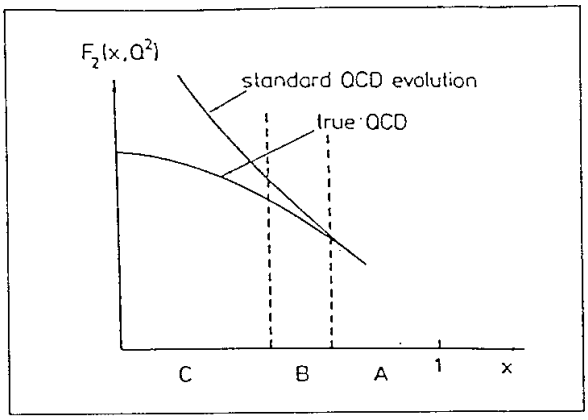

Figure 2.9: *Predicted behaviour at small x of the structure function. Labels A, B and C denote the region of perturbative QCD, the transition region and the nonperturbative region, respectively.*

bars are the statistical errors for a luminosity of $5\,\mathrm{pb}^{-1}$ and the full bars include a systematic error of 2% added in quadrature[2]. There is an impressive improvement due to the extension of the kinematic range below $x = 10^{-4}$ and the increased lever arm in $\ln Q^2$, thus improving the measurement by a factor 3 to 4 even for those values of x which are accessible now.

Gluon Distribution and Longitudinal Structure Function

The exploration of the low x region will be of particular importance for the measurement of the gluon distribution function. At HERA there are various ways to determine xG, namely the study of the QCD evolution of F_2 , the measurement of the longitudinal structure function and the evaluation of open charm or J/Ψ production. The gluon structure function is a common objective of the CST and the BST.

The dominance of the gluon term in the F_2 evolution equations can be utilized to determine $xG(x,Q^2)$ from the $F_2(x,Q^2)$ measurements which will cover a very wide range in the Q^2, x plane [35]. A fit of Λ_{QCD} and xG should allow distinguishing between different predictions for the low x behaviour of xG. The extension of the Q^2 range by the BST will improve the measurement of xG via the F_2 evolution as compared to the existing detector [36].

The measurement of the ratio $R = F_L/2xF_1$ is another way to determine the gluon distribution, since it dominates the evolution equation of the longitudinal structure function F_L at low x [37]. At small x the ratio R is predicted to be large as compared to the situation of previous deep inelastic experiments which measured R at $x \geq 0.05$ [26]. The experimental determination of R is necessary if one wants to determine F_2 to better than 15% accuracy at very low x and $y > 0.5$.

The R measurement requires accessing high values of y since R enters the one-photon exchange cross section with a weight factor y^2 according to

$$\frac{d^2\sigma}{dxdQ^2} = \frac{2\pi\alpha^2}{Q^4 x} \cdot \left[2(1-y) + \frac{y^2}{1+R}\right] \cdot F_2(x,Q^2). \tag{2.12}$$

[2]Recent data from the NMC [34] collaboration indicate that F_2 may be somewhat less steep than predicted by the B^- parametrization.

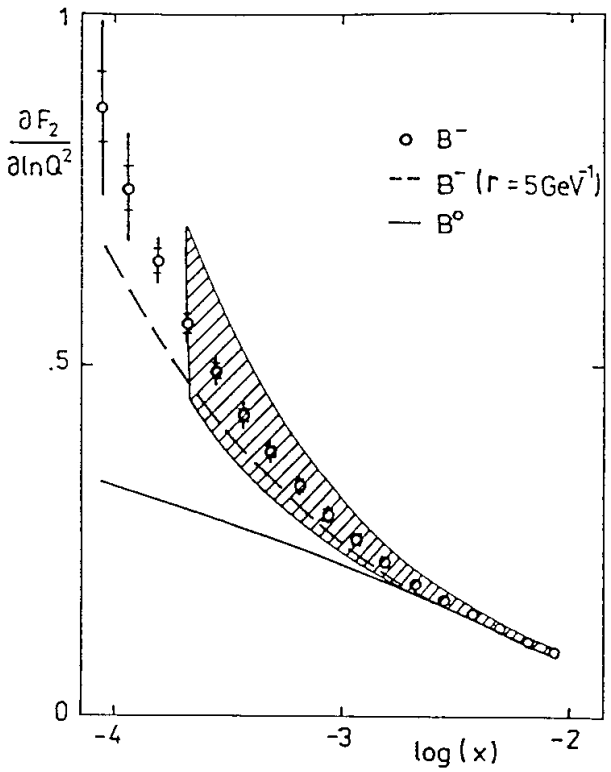

Figure 2.10: *Logarithmic derivative of F_2. Shadowed region: achievable statistical and systematical accuracy with the present H1 detector. Points: simulation of the measurement with the BST. The points follow the behaviour of the parametrization B^- of [31] which assumes the gluon and quark distributions to diverge as $1/\sqrt{x}$. The inner errors denote the statistical error for full detector efficiency for a luminosity of 5 pb^{-1}, the length of the bars representing the total error with a 2% systematical error added in quadrature. Solid curve: B°, a parametrization assuming the distributions to be constant as x tends to zero; Dashed curve: B^- with weak ($r = 5\ GeV^{-1}$) shadowing included.*

At low x, high values of y are obtained only when the energy of the scattered electron is small. Due to the large rate of low energetic particles (pions from photoproduction [38] and electrons from charm decays [39]) it is difficult to measure inelastically backward scattered electrons with energies of the order of 5 GeV. The BST provides two features for approaching the larger y region: the trigger with pad detectors is fully efficient down to low momenta [40] and the r-strip detectors measure the polar angle independently of the reconstruction of the primary vertex. Presently polar angles above 170° can only be measured by combining a point in the Backward Proportional Chamber with the z of the vertex position. Thus one depends on the description of the hadronic final state at very low x which is theoretically not well understood. The electron identification without the reconstruction of track segments is not sufficient to meet precision requirements.

Figure 2.11 shows a simulated R measurement with $E_e = 30$ GeV and two proton beam energies [3] $E_p = 400$ GeV and $E_p = 820$ GeV.

[3]The final measurement of R will have to include measurements at more than two enery settings. The main conclusions, however, do not depend on the chosen set of energies. An optimization of the R measurement including a discussion of systematic error sources has been presented in [41].

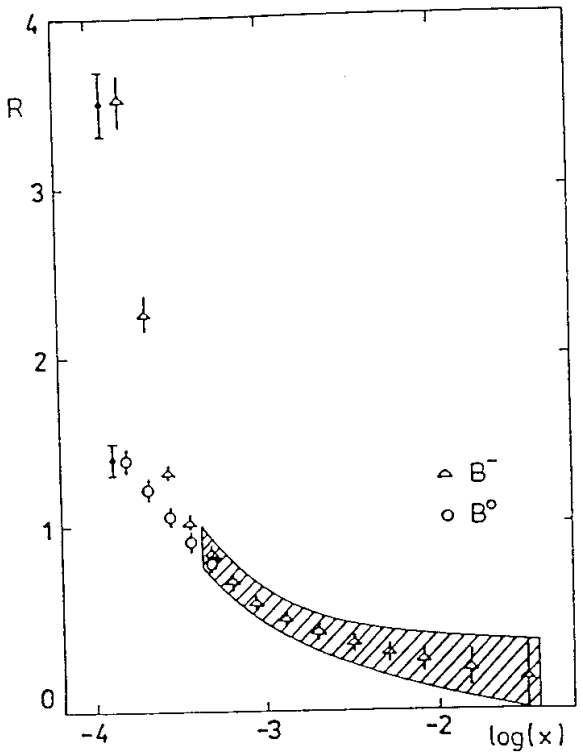

Figure 2.11: *Statistical accuracy of the ratio* $R = F_L/2xF_1$ *with the present H1 detector (dashed region) and with the BST using the leading order QCD expression for* F_L *[31] for two proton beam energies and luminosities of* 50 pb^{-1} *each. The separate error bars on the left illustrate the effect of a 1% relative luminosity error.*

The triangles in figure 2.11 follow the behaviour of the parametrization B° [31] whereas the open points represent the shape of R as calculated with B^-. The errors represent the statistical accuracy for a luminosity of 50 pb^{-1} at each energy setting. The dashed region shows the estimated statistical accuracy with the present H1 detector. The dominant systematic error source of this measurement is the relative normalization. Luminosity measurements and the adjustment of the data sets at different energies at low y allow to control the relative luminosity error at the per cent level. The R measurement is improved by the BST because the acceptance can be extended to lower x (see figure 2.11) and also to higher y ($y_{max} = 0.8$ instead of 0.7 at present). Large values of R would represent a strong violation of the Callan-Gross relation [42] and resuscitate the theoretical debate about the various contributions to F_L.

2.5 BST Design Parameters

It is foreseen to build the BST in two phases. In the first phase (BST-1), four disks of silicon detectors complement the present backward proportional chamber and electromagnetic calorimeter (BPC and BEMC). The BST-1 is equipped with silicon detectors having curved strips at constant radius (r-strip detectors) to measure the polar angle of the scattered electron and with silicon pad detectors realizing the novel first level trigger (L1) on low Q^2 events, see figure 2.12. The realization of the second phase (BST-2) is linked to the anticipated replacement of the BPC

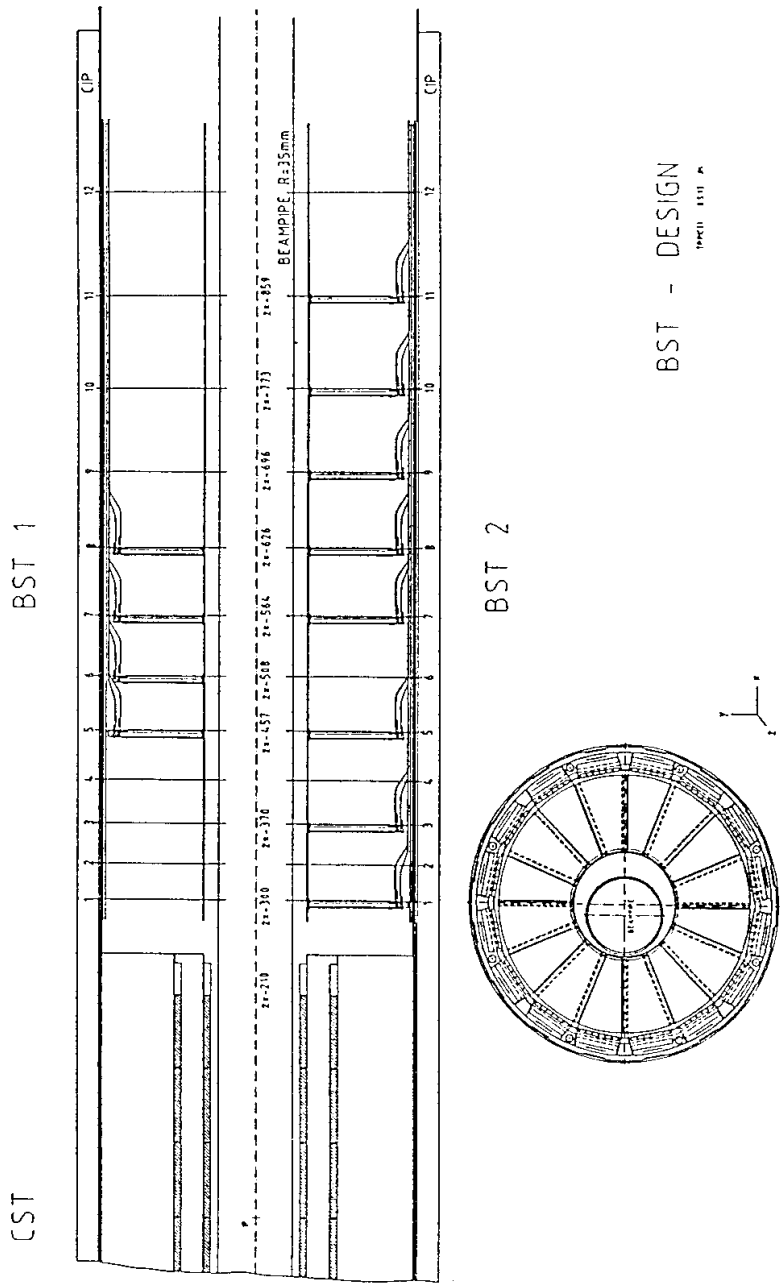

Figure 2.12: *View on the Backward Silicon Tracker (top: BST-1, bottom: BST-2). The x-y cross section illustrates the 16-fold subdivision φ and the excentricity of the beam pipe with respect to the interaction region and the BST.*

and the BEMC by new backward detectors which are necessary to further extend the acceptance and to ensure a better absolute energy calibration. In order to accept events in a polar angle range from the innermost calorimeter edge to the CJC at $\theta = 165°$, the BST-2 comprises eight disks of silicon detectors. In addition it is foreseen to add a third layer of silicon detectors to each of the disks, which have radial strips at constant azimuth (φ strip detectors). They will determine the charge and the transverse momentum of particles in the backward region, enabling to reduce the photoproduction background and to measure the hadron energy flow.

ϑ Resolution

The contribution of the BST to the x and Q^2 resolutions should not extend the one of an upgraded backward electromagnetic calorimeter, i.e. a few per cent. The resolutions are derived from the leptonic energy and angle uncertainties as:

$$\begin{aligned}
\frac{\delta Q^2}{Q^2} &= \frac{\delta E_l}{E_l} \oplus \tan(\frac{\vartheta}{2}) \cdot \delta\vartheta \\
\frac{\delta x}{x} &= \frac{1}{y} \cdot \frac{\delta E_l}{E_l} \oplus (\tan(\frac{\vartheta}{2}) + (\frac{1}{y} - 1) \cdot \cot(\frac{\vartheta}{2})) \cdot \delta\vartheta \\
\frac{\delta y}{y} &= (1 - \frac{1}{y}) \cdot \frac{\delta E_l}{E_l} \oplus (\frac{1}{y} - 1) \cot(\frac{\vartheta}{2}) \cdot \delta\vartheta
\end{aligned} \tag{2.13}$$

where the symbol $\oplus$ denotes addition in quadrature. A few observations are important here:

- Both the x and the y resolution suffer from a $1/y$ term, i.e. the electron without the current jet can be used only above $y \simeq 0.05$ [43] to determine the double differential cross section.
- Contrary to x and y one can measure Q^2 over the full range in y. It can be very important to perform a combined measurement using electron and jet information in those regions where the hadron measurement is not accurate enough [44, 45].
- The angular measurement affects the Q^2 and x resolution with a weight $\tan(\vartheta/2)$. The largest angle to be detected is 177°, taking into account the interaction vertex smearing and assuming the new calorimeter to be efficient up to 176°. At this angle the ϑ contribution to the resolutions is weighted by a factor of almost 40, i.e. we have to require a ϑ measurement accuracy of the order of 1 mrad in order not to dominate the resolution.
- The BST has to determine the direction of the scattered electron independently of the reconstruction of the interaction vertex (see figure 2.13). This requirement determines the pitch of the r-strip detectors to be about 100 μm.

Figure 2.14 shows a calculation of the expected x, y and Q^2 resolutions with the BST which are of the order of 5% to 10%.

φ Resolution

We propose to implement φ-strip detectors in phase 2 to measure the momentum of charged tracks in the backward region from $\vartheta = 165°$ to 175°. This is motivated by the following physics issues:

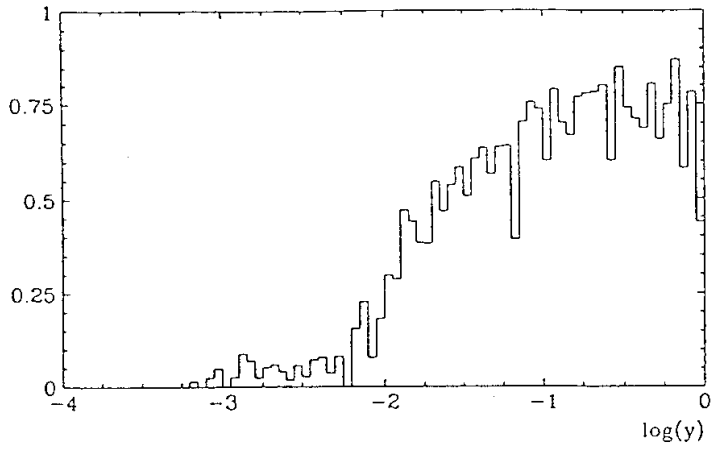

Figure 2.13: *Efficiency of reconstructing the vertex position as a function of* $\log(y)$ *with the present detector using a Monte Carlo simulation of events with radiative corrections. To reconstruct the vertex at least 2 tracks and a hit in the BPC are required. At* $y \leq 0.03$ *the efficiency drops because the hadron energy flow is concentrated at small angles with respect to the proton beam direction.*

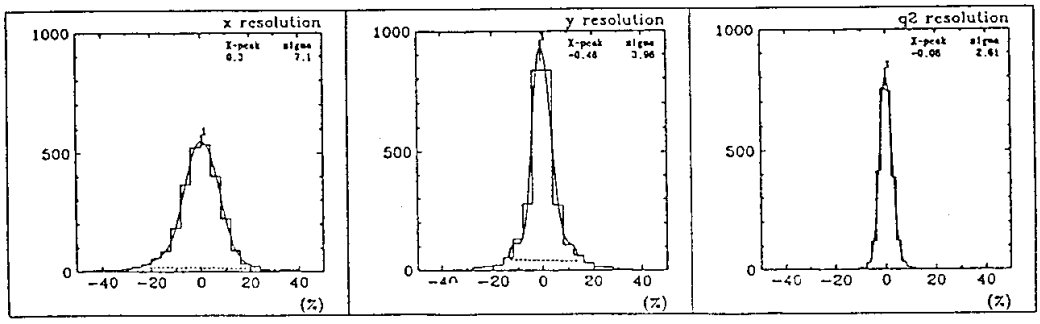

Figure 2.14: *Resolutions of* x, y *and* Q^2 *averaged over the BST acceptance range for a sample of generated events with* $y \geq 0.1$.

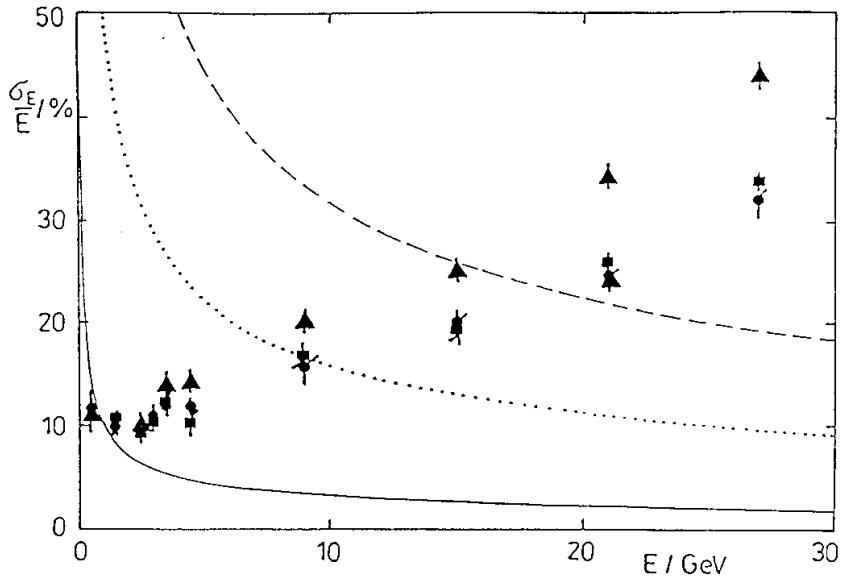

Figure 2.15: *Energy resolutions for a sample of events tracked with HISIM through the BST. Points: resolutions achievable with the BST for a φ pitch of 0.5, 1 and 3 mrad, the best resolutions at high E corresponding to the finest pitch. Curves: calorimetric measurements with resolutions of 10, 50, and $100\%/\sqrt{E}$ (solid, dotted and dashed curves, resp.).*

- The identification of scattered electrons will be substantially improved at momenta below 10 GeV/c by comparing the BST and the calorimetric responses (E/p matching).
- A measurement of the electron charge allows to subtract the charge-symmetric background from photoproduction and heavy quark decays. This technique was used for the R measurements at SLAC [26] and is very important to extend the y range beyond $y = 0.7$.
- Hadron energy flow measurements are needed to extend the acceptance for deep inelastic scattering events to values of y below 0.05.
- Hadron measurements at large angles will allow to analyze the spectator jet in resolved photon events.

We have performed a simulation of the BST with φ-strip detectors to obtain the momentum resolution. The results are summarized in figure 2.15 and compared to the energy resolution for different calorimeters (curves for 10, 50 and $100\%/\sqrt{E}$). The p_t measurement uses a vertex-constrained fit and the transverse size of the luminous region at HERA is taken into account for the resolution. At momenta below a few GeV, the resolution of the p_t measurement is dominated by multiple scattering. The beam pipe contributes about 40% of the material with a weight $\sim 1/\sin\vartheta$. The requirement to determine the charge of the electron up to 15 GeV suggests to choose an azimuthal angular pitch of 1 mrad (see figure 2.15).

This proposal presents a design of the φ-strip detectors as a basis for prototype development. The final design will be optimized in conjunction with the new backward detectors.

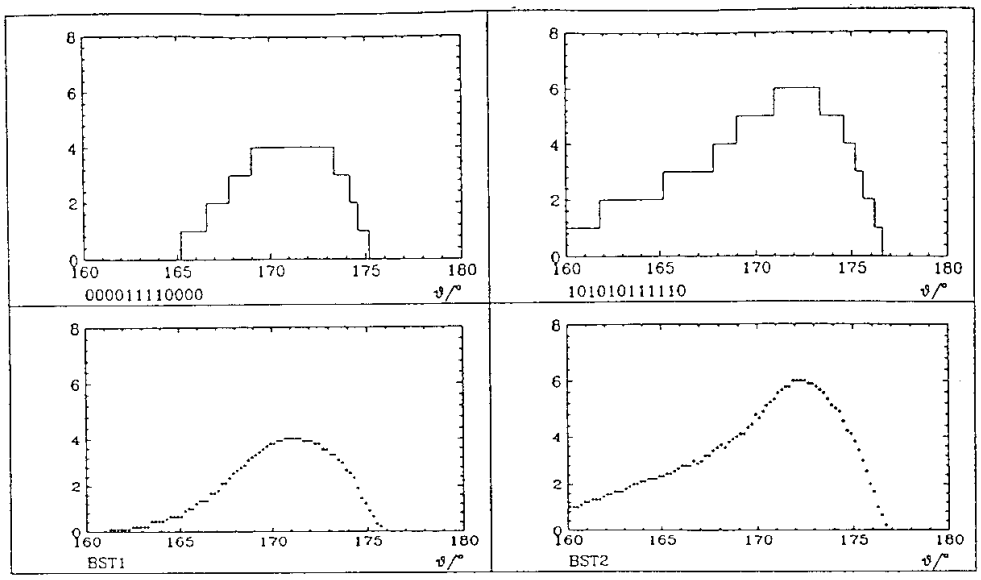

Figure 2.16: *Average number of hits for a) BST-1 and b) BST-2 without (top) and with (bottom) an interaction vertex smearing of* ± 100 *mm versus polar angle.*

BST Geometry

The geometry of the Backward Silicon Tracker is determined by the following constraints:

- The BST-1 extends the electron tracking from the edge of the acceptance of the central inner z-chamber at 169° to the region of the innermost BEMC stacks at 174°. The BST-2 covers the region from 167°, where the track reconstruction of the CJC becomes inefficient, to the inner edge of a future backward calorimeter at 176°. For pattern recognition and track reconstruction, hits in 4 disks are required. Therefore, BST-1 consists of 4 disks whereas BST-2 requires 8 disks (see figure 2.16).

- To keep the BST trigger simple, the BST disks are arranged concentrically around the beam line with an inner radius of 50 mm. The outer radius is limited to 120 mm by the inner proportional chamber (CIP) and space needed for the cabling of the CST.

- The size of a detector fabricated from a 4 inch silicon wafer and the available radial space suggest a 16 fold subdivision of the BST in φ. From a simulation of deep inelastic events in the BST region we find that less than 1% of the hadrons traverse the same sector ($2\pi/16$) as the scattered electron (figure 2.17). The mean multiplicity of hadrons scattered backwards is between 1 and 2, which eases pattern recognition and triggering.

- The BST trigger detectors will be radially subdivided into $n = 8$ rings. The requirements of forming trigger roads pointing to the vertex and having an identical design for all disks can be satisfied if the z positions of two consecutive BST disks follow the relation:

$$z_{i+1} = z_i \cdot \sqrt[n]{\frac{r_{max}}{r_{min}}} \tag{2.14}$$

  where r_{min} and r_{max} denote the inner and outer radius of the sensitive detector region. The first possible position of a BST disk is at $z_1 = -300$ mm as determined by the length

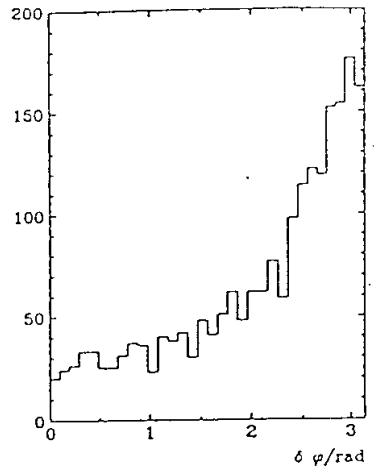

Figure 2.17: *Distribution of differences of azimuthal angles between the scattered electron and hadrons in the backward region. The binning corresponds to a 32 fold subdivision in φ.*

of the CST. The sequence of radii is then given by:

$$r_k = r_{min} \cdot (\frac{z_2}{z_1})^k. \tag{2.15}$$

Table 2.3 contains the z-positions and the radial subdivision of the pad detectors. A pad detector is shown in figure 2.18.

i	1	2	3	4	5	6	7	8	9	10	11	12
z_i [mm]	-300	-333	-370	-412	-457	-508	-565	-628	-697	-775	-861	-957
BST-1					•	•	•	•				
BST-2	•		•		•		•	•	•	•	•	
k	1	2	3	4	5	6	7	8				
r_k [mm]	52.3	58.1	64.6	71.8	79.8	88.6	98.5	109.4				

Table 2.3: *z positions and radial subdivision of the BST pad detectors. The geometry is determined by setting: $z_1 = -300\,mm$, $r_{min} = 52.3\,mm$, $r_{max} = 121.6\,mm$ and the number of rings to 8.*

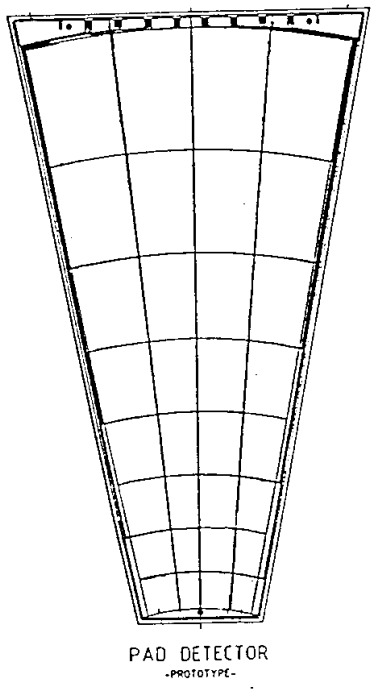

Figure 2.18: *Design of the pad detectors. The length of the detector is 74 mm. The 4-fold subdivision in φ reduces the capacitance.*

2.6 BST Trigger Concept

The present trigger on scattered electrons uses energy thresholds set in the Backward Electromagnetic Calorimeter (BEMC) and the Time-of-Flight (TOF) decision. The latter can be used as a veto against beam-wall and beam-gas background events or as a positive trigger on penetrating hadrons. At low electron energies (high y) the BEMC trigger becomes inefficient because a threshold of 5 to 10 GeV has to be set for background suppression. At angles above $\vartheta \simeq 172°$ one reaches the edge of the acceptance region of the present BEMC as shown in Figure 2.19a. The 'positive TOF' (PTOF) trigger decision (figure 2.19b) improves the acceptance at large ϑ and high y but it depends on the hadronization at very low x.

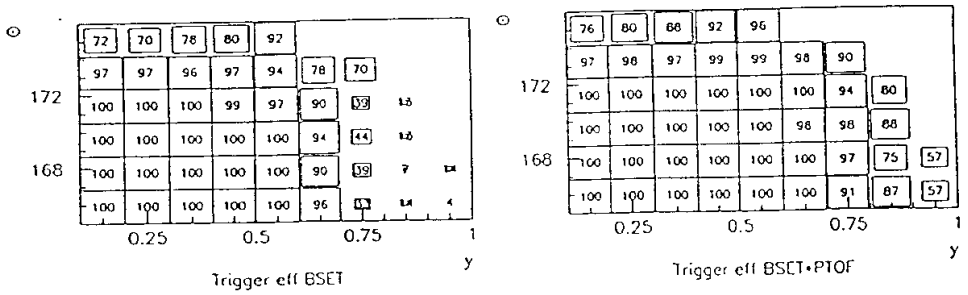

Figure 2.19: *Trigger efficiencies: a) BEMC trigger ('BSET' with a threshold of 4 GeV and a cluster threshold of 8 GeV) and b) BEMC × PTOF [48]. The events have been generated according to the distribution MTB2 [49].*

A dedicated level 1 trigger for electrons in the backward region is therefore necessary. It should:

- extend the acceptance in the $\vartheta - y$ plane and allow to run with lower BEMC thresholds,
- reduce the background trigger rate caused by the proton beam and synchrotron radiation,
- establish a redundancy of the low Q^2 trigger acceptance, in order to determine the trigger efficiency directly from the data, which is particularly important in a region of large backgrounds, and
- allow for a large z-vertex position smearing around the nominal interaction point.

The proposed trigger uses the signals from the pad detectors and requires straight tracks inside one φ-sector which orginate from the interaction region. A detailed design study of the BST trigger has been presented recently [40]. Each track coming from the vertex crosses a number of pad detector rings. This generates a pattern of ring numbers. For example, the BST-1 pattern (2 3 4 5) describes a track which enters the second ring in the first disk, traverses through ring 3 of the second disk and finally leaves the BST after crossing ring 5 in disk 4. Valid patterns ('masks') belong to tracks pointing to the interaction region.

Figure 2.20 shows the trigger efficiency calculated with H1SIM as functions of the number of

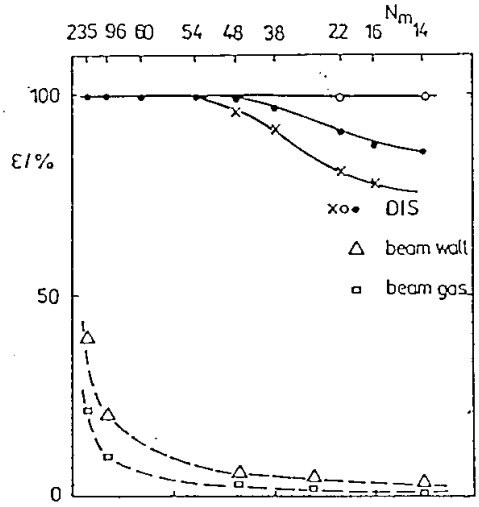

Figure 2.20: *Trigger efficiency as a function of the number of allowed ring patterns N_m. The solid curves refer to deep inelastic scattering events with a vertex smearing of 0, ± 100, and ± 200 mm for* o • × *respectively.*

masks. It can be seen that the inclusion of 50 different masks ensures nearly full efficiency even if the z-position of the interaction vertex is smeared over 400 mm. Only a small fraction of the beam gas and beam wall events hit the BST and very few of them generate a valid trigger pattern. The trigger also includes a cut on the hit multiplicity to further reduce the background. Deep inelastic scattering events are not affected by this cut since they have only few tracks in the BST region. However, the BST trigger cannot run stand alone since the proton beam induced background rate is about two orders of magnitude larger than the DIS rate. The hit detection efficiency can be monitored with the data because of the large cross section for DIS events and since all pads within the ϑ acceptance region are hit by tracks crossing 4 disks.

Chapter 3

Radiation Background

3.1 Limits

Radiation Damage to Silicon Detectors and Front-end Electronics

Single sided, AC-coupled silicon strip detectors tolerate total doses of a few Mrad from ionizing radiation and fluences of several $10^{13}/cm^2$ from neutron radiation [51]. Similar radiation hardness was demonstrated recently for double sided detectors [52]. Our readout electronics is fabricated in a $2\,\mu m$ CMOS process which is not designed to be radiation hard. However, test transistors and protoype amplifiers were found to be functional up to a dose of 150 krad from a Co^{60}-source (see section 5.1). A minimum ionizing particle deposits an average energy of 117 keV in $300\,\mu m$ of silicon. The energy deposition from an interacting synchrotron radiation photon is typically 50 keV. The fraction of interacting photons depends on the energy spectrum, but is generally less than 10%. The mass of all silicon detectors in the CST and BST is about 400 g. Therefore, a dose rate of 15 krad/year (for a lifetime of 10 years for the front-end electronics) corresponds to about 30 hits per bunch crossing in the silicon tracker and to a photon flux of $4 \cdot 10^9/s$.

Background Hits in the Silicon Tracker

Heavy flavour events produce about 15 hits in the CST. With an average cluster size of 2 strips and double sided readout, the channel occupancy is about 0.001. From pattern recognition requirements the number of continuous background hits per event should not be much larger. This corresponds to a dose rate of about 10 krad per year of operation. The trigger scheme for the BST can tolerate a few background hits per event, leading to about the same dose rate limit.

Background in the Central Jet Chamber (CJC)

The pattern recognition procedure in the CJC can tolerate a few hundred randomly distributed background hits per event, where one event extends over 15 bunch crossings for a maximum drift length of 45 mm. The level 1 track trigger sets a similar limit. The average energy of scattered synchrotron radiation photons which reach the CJC is about 80 keV, corresponding to an interaction probability of 3% in 60 cm of argon gas. Therefore, a photon flux of $7 \cdot 10^9$ /s can be tolerated in the CJC. This limit is similar to the limits set by the silicon tracker itself.

To prevent wire ageing effects, a total collected charge of about 1 C/cm should not be exceeded.

Using the wire length (215 cm), the gas gain (10^4), the number of sense wires in the CJC (2560), the average energy of interacting photons (80 keV) and the ionization energy of Argon (25 eV) one calculates a limit of 100 hits per bunchcrossing for a lifetime of 10 years.

3.2 Direct Synchrotron Radiation

The electron beam is bent by 10 mrad in a group of dipole and off-axis quadrupole magnets placed between 24 m and 5.6 m from the interaction point (see figure 3.1). The average bending radius is 1400 m. At 35 GeV beam energy and the design current of 60 mA, the synchrotron radiation power emitted in this section is 9.5 kW. The total number of photons radiated is $3 \cdot 10^{18}$/s and the spectrum has a characteristic energy of 67 keV. It is necessary to reduce the photon flux by 10 orders of magnitude before it reaches the central tracking detectors. This is achieved by a set of collimators and absorbers, some with a special low albedo coating, which

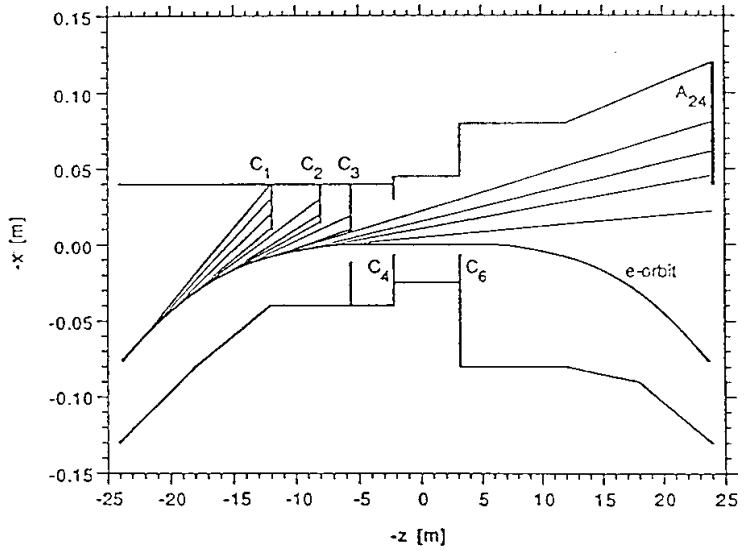

Figure 3.1: *Direct synchrotron radiation in the HERA ring plane. Note the different scales for the z and x-axes.*

allow only photons to reach the central detector that scattered at least twice off collimators . Collimators exposed to direct radiation (C_1, C_2, C_3 and A_{24}) are placed as far away from the detector as possible to reduce the solid angle for scattered photons.

The new narrow beam pipe must not be hit by direct radiation. A computer program was used, which transports individual electrons through the magnet optics (stepsize 1 cm) and follows photon rays inside the beam pipe. Figure 3.2 shows a profile of the direct synchroton radiation in the transverse plane at the interaction point. The vertical spread is determined by the angular divergence of the electron beam while the horizontal spread is caused by the deflection in the bending magnets. The limit at $-x$ is given by the edge of collimator C_3, which is set at 12 mm from the beam axis. The simulation shows that a beam pipe with a radius of 35 mm and a horizontal offset of 10 mm is not hit by direct radiation.

The installation procedure for the silicon tracker requires that the narrow beam pipe extends to $z = -2.8$ m. Figure 3.3 shows the outer edge of the synchrotron radiation profile at -2.8 m as a

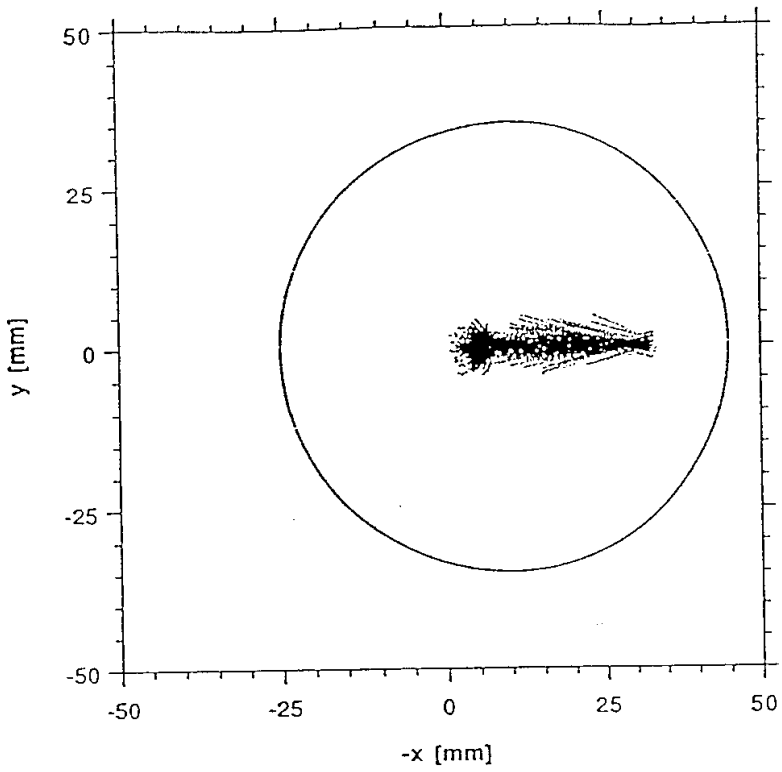

Figure 3.2: *Profile of the synchrotron radiation at the interaction point viewed along the proton direction. C_3 is closed to 12 mm. A beam pipe with a radius of 35 mm and a horizontal offset of 10 mm is drawn.*

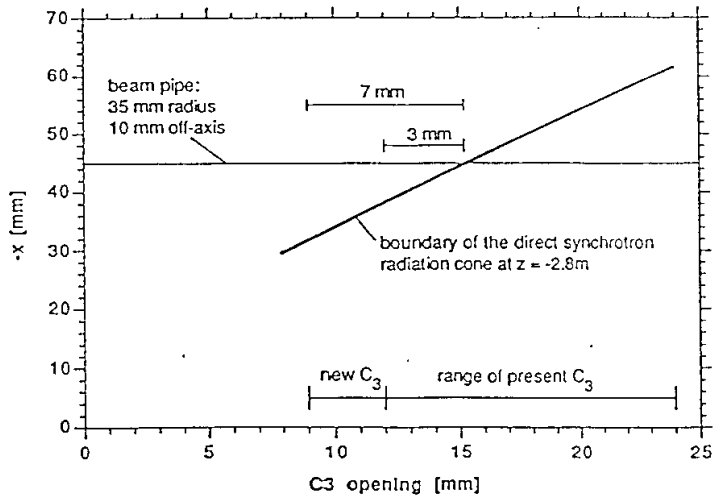

Figure 3.3: *Edge of the synchrotron radiation profile at $z = -2.8\,m$ as a function of the opening of C_3.*

function of the opening of collimator C_3. The new beam pipe is shadowed over its full length if C_3 is closed below 15 mm. The existing collimator can be closed to 12 mm. The present electron optics with a horizontal emittance of $7 \cdot 10^{-8}$ rad m at 35 GeV allows to close C_3 to 10 mm before the $10\,\sigma$ envelope of the electron beam is reached. Closing C_3 below 12 mm increases the safety margin against shifts in the beam position and radiation from the tails of the electron beam. Therefore, we propose to modify C_3 such that it can be closed to at least 10 mm.

At electron injection, C_3 has to be fully opened and the beam pipe is hit directly. However, at the injection energy of 12 GeV the radiated power is only 90 W and the spectrum is soft with a characteristic energy of 2.8 keV. Thus most of the radiation is absorbed inside the beam pipe. Furthermore, the drift chambers can be switched off during injection. Before the electrons are accelerated C_3 must be closed. This scheme requires that protons are filled and accelerated first.

3.3 Scattered Synchrotron Radiation

The effect of scattered synchrotron radiation was simulated taking into account photoeffect and fluorescence, Compton scattering modified by atomic structure functions, and coherent scattering modified by atomic form factors. Secondaries were followed down to a cutoff energy of 1 keV. Similar studies have been performed for the ARGUS silicon vertex detector at DORIS [53] and the LEP detectors [54] which agree with measurements at the 50% level. We will verify the calculations with data from the first running period of HERA.

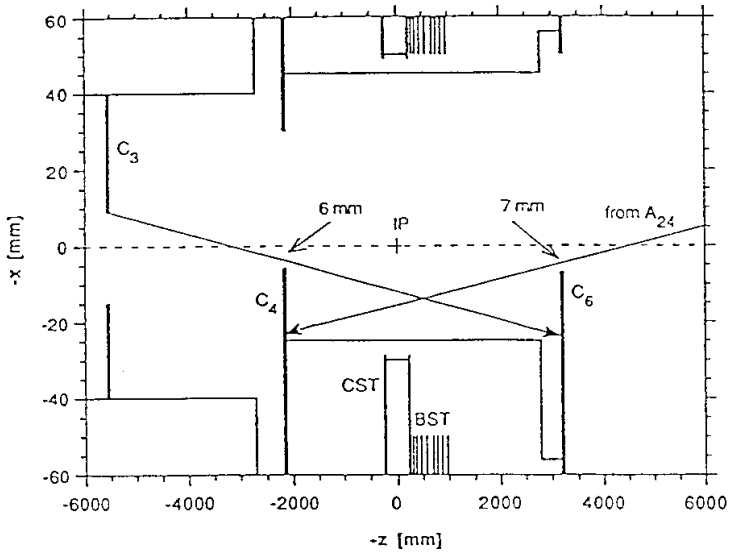

Figure 3.4: *Scattered synchrotron radiation in H1.*

The strongest sources of scattered radiation for the central detector are the edge of collimator C_3 and the absorber A_{24}, placed 24 m downstream (see figure 3.4). At present, collimators C_4 and C_6 shield the central beam pipe against scattered radiation from these two sources. This shielding is incomplete for any beam pipe radius smaller than 80 mm. Collimator C_4, placed at $z = 2.14$ m, is not movable. Its inner edge has a distance of 25 mm from the beam. We propose to upgrade C_4 with a movable tungsten plate which can be closed down to 7 mm. The $10\,\sigma$ envelope of the electron beam at this position is 5 mm. During injection, the tungsten plate has

to be opened to 25 mm. The mass of the plate is less than 500 g. Without this upgrade the background rate in the CJC at 35 GeV is about 40 hits per event (15 bunch crossings) which approaches the limit set by the CJC pattern recognition.

Collimator C_6 at $z = -3.14$ m is presently movable in the range from $x = 50$ mm to $x = 25$ mm. It has to be upgraded to reach $x = 7$ mm to reduce the radiation backscattered from absorber A_{24}.

With the three upgraded collimators (C_3, C_4, C_6) the shielding will be better than at present, even with the new beam pipe in place. The expected dose rate from synchrotron radiation in the silicon detectors is about 0.1 krad/year.

3.4 Hadronic Background

With $2 \cdot 10^{13}$ protons stored in the beam and a vacuum of $3 \cdot 10^{-9}$ Torr, the expected rate for beam-gas events is 3 kHz/m. Standard H1 beam-gas and beam-wall event files were used as input for the detector simulation package H1SIM, which included the geometry of the silicon tracker. On average, 0.02 hits per bunch-crossing were seen in the silicon detectors, which corresponds to a radiation dose of 10 rad/year.

The total ep cross section (about 200 μb for photoproduction, 5 μb for 2-jet production) generates a dose rate of about 0.2 rad/year in the silicon detectors. We conclude, that the hadronic background does not pose a problem in terms of radiation damage or occupancy.

Chapter 4

Silicon Detector Specifications

4.1 Double Sided Strip Detectors for the CST

Inspired by the demands from particle physics experiments the technology for the fabrication of silicon strip detectors has rapidly improved in recent years by applying the state-of-the-art in semiconductor processing. Single-sided, DC-coupled strip detectors were introduced in 1980. Detectors with integrated coupling capacitors and bias resistors were first produced in 1987. Double sided silicon strip detectors have been successfully operated by the ALEPH collaboration at LEP since 1990. The DELPHI collaboration is presently upgrading their silicon vertex detector to use double sided detectors which include a second metal layer for readout lines. Other projects using double sided detectors are underway at L3, CLEO-II and D0.

Figure 4.1 shows a sketch of a double sided detector. Our general specifications for the detectors are:

- 25 μm pitch, every second strip is read out.
- Wafer thickness 300 μm.
- Full depletion voltage less than 80 V.
- Leakage current less than 10 nA per strip at a bias voltage 10% above full depletion for 99% of all strips.
- Interstrip resistance on the n-side at least 3 MΩ.
- Readout strips are AC-coupled to the amplifiers. Coupling capacitance about 10 pF per cm strip length.
- Integrated bias resistors for each implant strip on both sides.
- Double metallization on a thick dielectric for readout on the n-side.

There are a few suppliers for double sided strip detectors which differ in some technological aspects [55]. A major issue in recent years was the interstrip insulation on the n-side. Since the n-strips are embedded in a depleted n-substrate, any positive charges trapped at the surface reduce the interstrip resistance. A net positive charge from holes trapped at the Si-SiO_2 interface usually remains after the fabrication and further holes are generated in a radiation environment. Two insulation methods are available. ALEPH used detectors with intermediate p-blocking

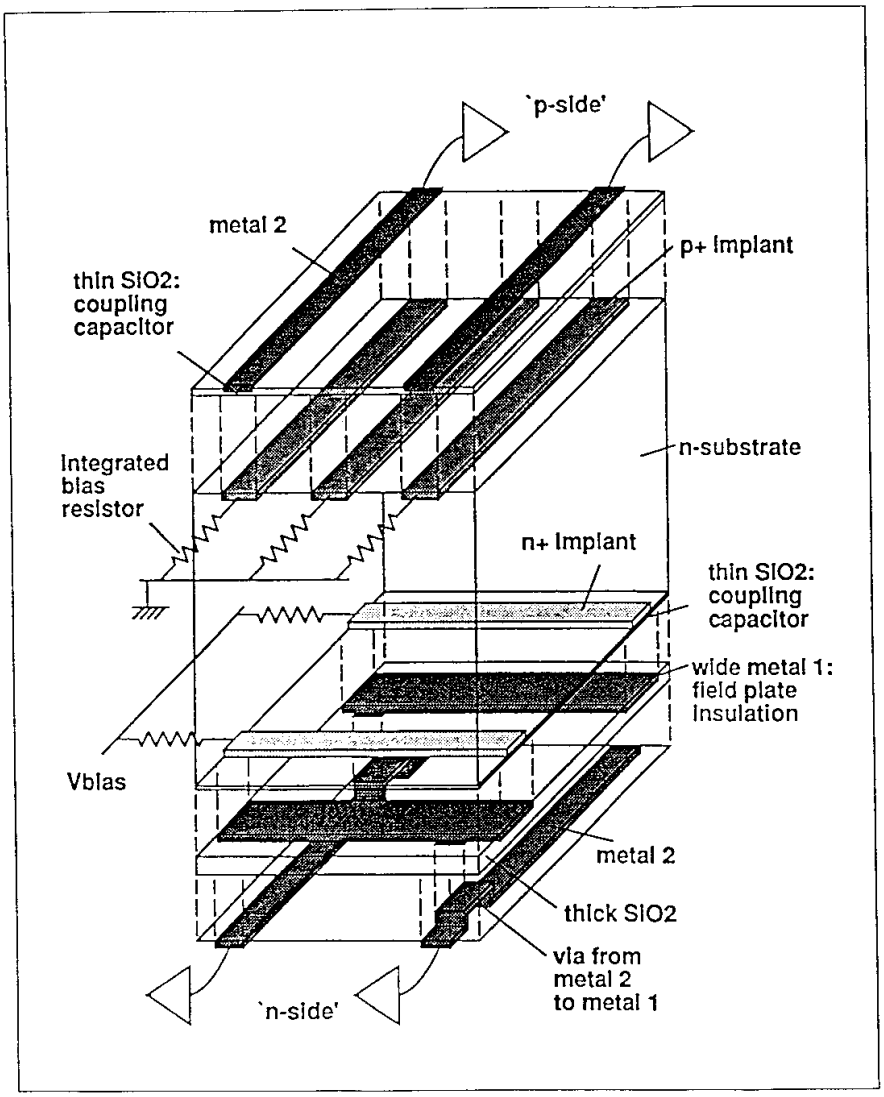

Figure 4.1: *Perspective view of a double sided silicon strip detector. The surface layers are shown in an exploded view.*

strips, with good results. The DELPHI upgrade uses a field plate insulation method, which now gives equally good separation and radiation hardness. A simulation [56] shows that the interstrip capacitance may be lower for the field plate method, making it the preferred choice.

The amplifier cannot absorb large leakage currents at the input and has to be capacitively coupled to the strips. The leakage current is then absorbed by biasing resistors which are integrated on the detectors. Bias resistors can be made of polysilicon on both sides. Another solution with fewer processing steps uses punch-through biasing on the p-side and accumulation layer resistors on the n-side. In high radiation environments like the SSC or LHC, polysilicon resistors are preferred because of their better radiation hardness. For the HERA environment all options have sufficient radiation stability. The coupling capacitors can either be integrated on the strip detectors or placed on a separate chip. A separate capacitor chip requires a few centimeters of space and one additional bond per channel. This solution is less expensive, since strip detectors without integrated coupling capacitors can be produced with a higher yield. In both cases, the stability of the coupling capacitors on the n-side, where the full bias voltage is applied, is a major concern. If one capacitor breaks, the amplifier immediately saturates and a large leakage current flows. As a result, the electric field in the detector is distorted over a region of several hundred μm. On a prototype double sided detector we observed that one broken capacitor renders up to 15 strips unusable. However, capacitors develop pin-holes only during fabrication and are stable thereafter. It is therefore possible to identify broken channels during assembly and not to bond them to the amplifiers. Furthermore it is possible to raise the ground potential for the amplifiers on the n-side to the full bias voltage. If a capacitor breaks, the electric field is not distorted and only one channel is lost. However, this makes the design of the double sided hybrid and of the power supplies more difficult. A decision will be made after tests on prototype detectors.

4.2 r-Strip Detectors for the BST

All 3 types of detectors for the BST are wedge shaped, see figure 4.2. The readout chips are located at the outer circumference in order to reduce the amount of scattering material between the disks.

The specifications for the r-strip detectors are:

- Wafer thickness about 300 μm.
- Depletion voltage below 80 V.
- Strip pitch 45 μm, every second strip is read out.
- AC coupled readout strips.
- Integrated bias resistors greater than 3 MΩ.
- Interstrip leakage currents below 100 nA.
- Second metal layer for readout lines on a thick dielectric.

The design of the r-strip detector is shown in figure 4.3. The strips extend in φ over $2\pi/16$ in order to gain a few mm overlap for adjacent sectors. Consequently, the sectors are staggered in z when mounted to a disk. This overlap is important for efficiency checks and alignment.

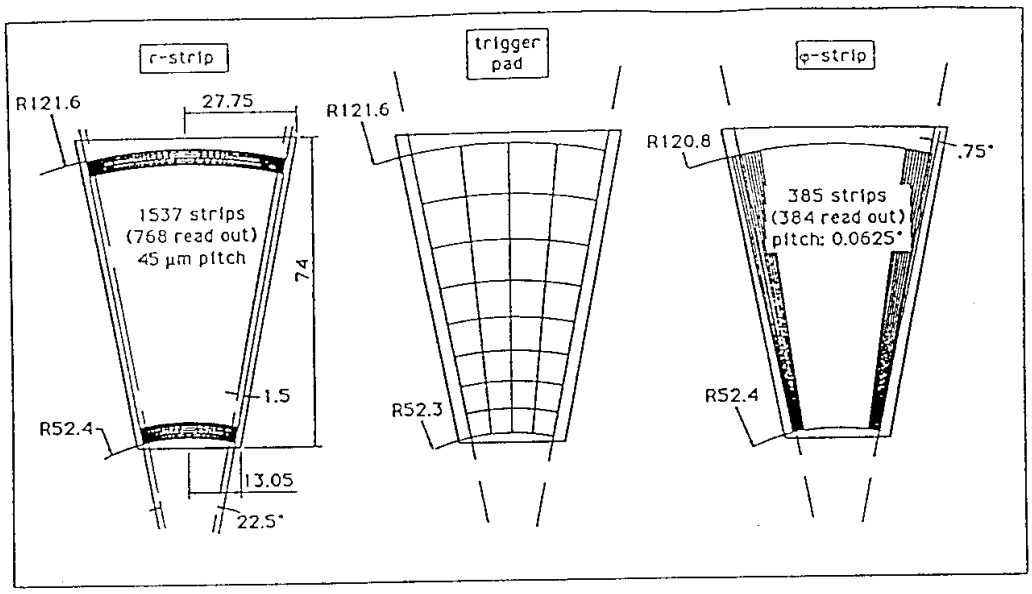

Figure 4.2: *Outline of the BST detector types. (a) r-strip detector, b) trigger pad detector, c) φ-strip detector. All types have identical mechanical dimensions. There are small differences in the active areas due to different technical requirements.*

4.3 φ-Strip Detectors for the BST

The dimensions of the φ-strip detector are given in figure 4.2 c. The radial strips have a length of 68 mm and an angular pitch of 1/16 degree corresponding to 58 μm pitch at the inner radius and 133 μm at the outer one, see figure 4.4. At each side there are 12 additional strips for overlap with adjacent sectors. The 384 strips are read out by 3 chips.

The strips are AC coupled and biased via integrated polysilicon resistors at the inner radius. All specifications given for the r-strip detectors apply here, except that a second metal layer is not required.

4.4 Trigger Pad Detectors for the BST

The sensitive area of the pad detectors is subdivided into 8 rings of 4 pads each, resulting in pad sizes between 14.3 and 175.0 mm^2. The wafer thickness (380 μm) is chosen to be larger than for the strip detectors in order to reduce the pad capacitance and to raise the amount of signal charge. The pads are biased either through the preamplifier input itself or by discrete components located on the readout hybrid. A metal line connects every pad to a row of bonding pads at the outer radius of the detector. These long traces impose a high parasitic load to the preamplifier. A special distributed guard structure between the readout lines has been designed which reduces the trace capacitances.

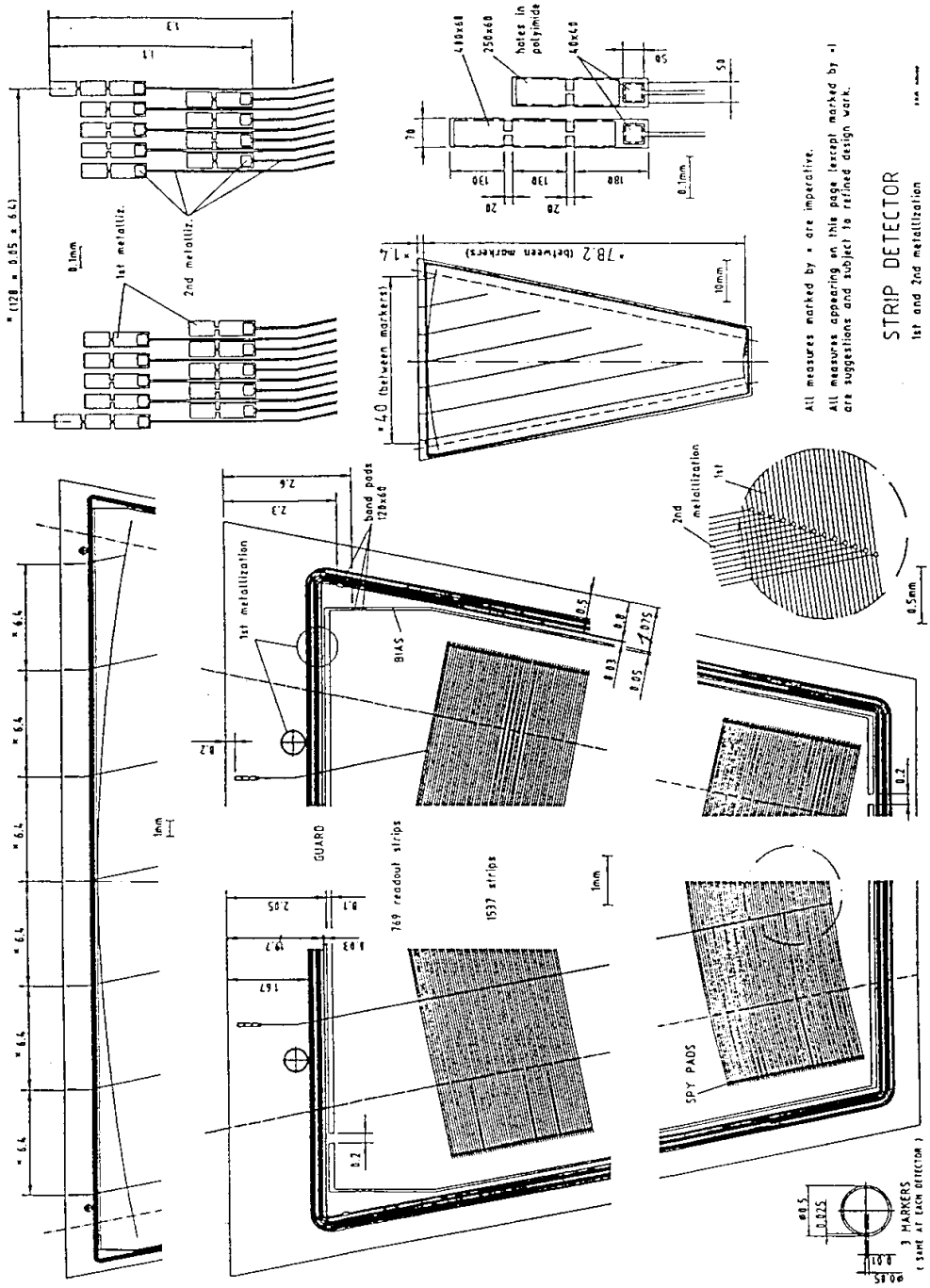

Figure 4.3: *Details of the design of the BST r-strip detector. The dimensions refer to the prototype detectors.*

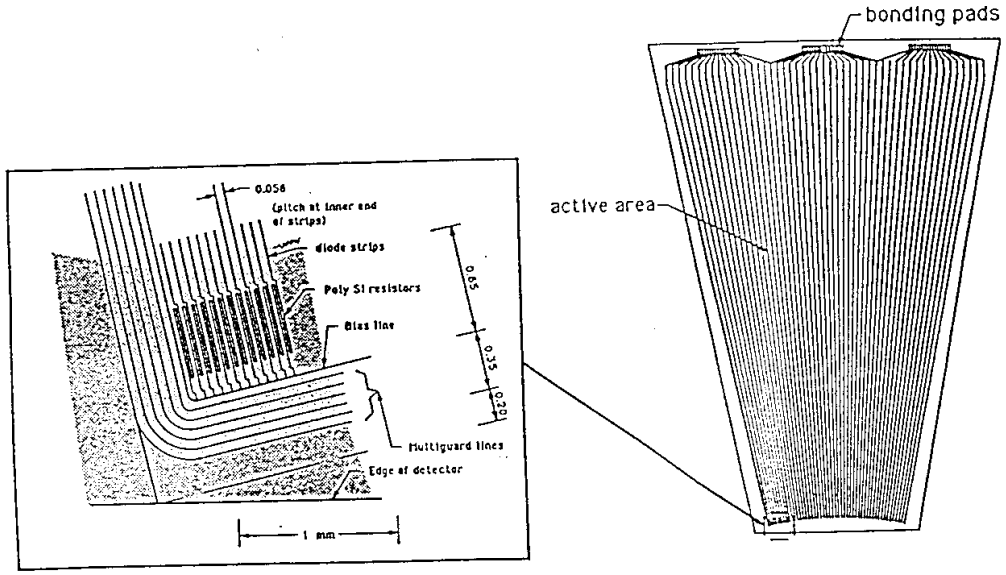

Figure 4.4: *Design of the BST φ-strip detetcor.*

Prototypes of the pad detectors have been manufactured and tested. The C-V curves of the largest and the smallest pads are shown in figure 4.6. The detectors have remarkably low leakage currents, see table 4.1.

A specific problem of detectors with large pad areas are crystal defects. Out of the 256 pads on eight prototype detectors we found 9 pads with either a high leakage current or a low interpad resistance. This fault rate has to be accepted for the series production. However, special masks can be added to the set of trigger patterns which take the defective pads into account.

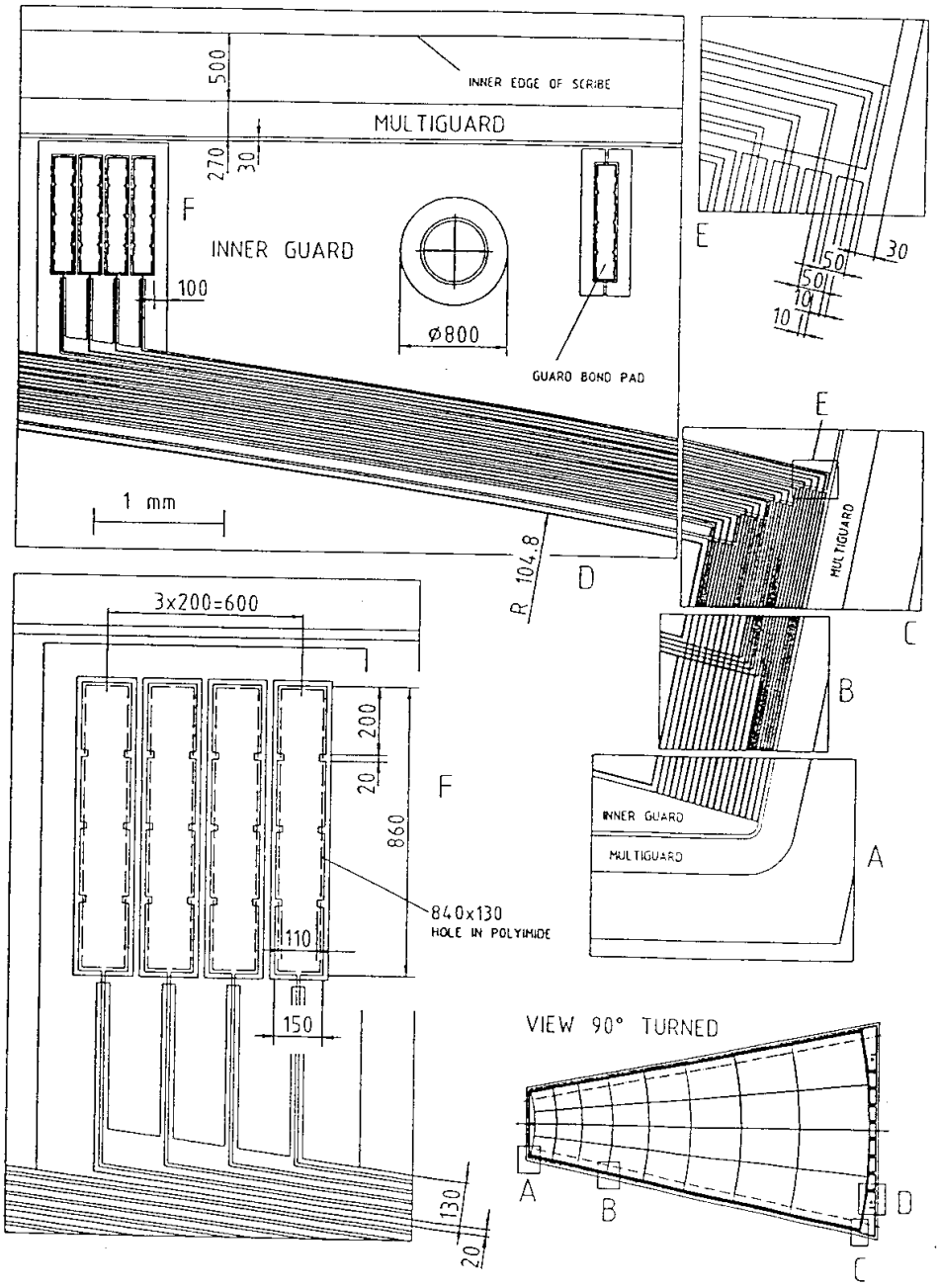

Figure 4.5: *Design of the BST pad detector*

Depletion Voltage		60 V
Leakage Current	whole detector	1.62 nA
	largest pad	0.39 nA
	smallest pad	0.012 nA
Capacitance	whole detector	715 pF
at full depletion	smallest pad	7.0 pF
	largest pad	48.7 pF

Table 4.1: *Measurements on pad detector prototypes*

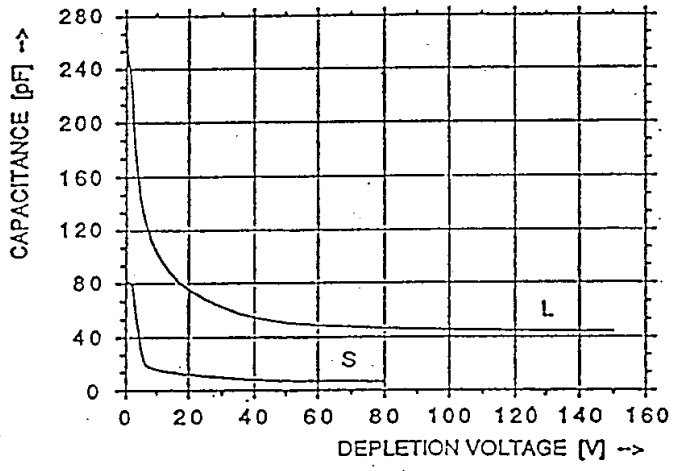

Figure 4.6: *C-V curves for BST pad detectors,* L *: largest pad,* S *: smallest pad*

Chapter 5

Readout Electronics

5.1 Amplifier and Pipeline Chip for Strip Readout

A new front-end readout chip for silicon strip detectors has been developed and prototypes have been successfully tested [58]. The chip is fabricated in a $2\,\mu m$ CMOS process [59]. It has 128 readout channels and is designed with a width of $44\,\mu m$ per channel. Each channel consists of a low noise, low power charge sensitive preamplifier followed by a multievent pipeline, which stores the analog signals of 32 consecutive bunch crossings. After a level 2 trigger, the pedestal subtracted analog signals are read out serially. With the prototype chips a read out speed of 2.5 MHz has been reached, thus allowing a 2000 : 1 multiplexing within the standard $800\,\mu s$ readout time of H1. The total power consumption of the chip including the pipeline running at 10 MHz is $300\,\mu W$ per channel.

Figure 5.1 illustrates the design of the amplifier and pipeline chip (APC). It requires 14 digital controls and 3 supply voltages. The charge sensitive preamplifier consists of a single gain stage with active load, which offers minimal power consumption for a given transconductance g_m of the input transistors. When operated with $280\,\mu W$ power per channel an equivalent noise resistance of $400\,\Omega$ is achieved. With an open loop gain of 80 a Miller capacitance of 25 pF is obtained. For load capacitances of similar magnitude the charge collection on the feedback capacitor is incomplete. The signal-to-noise performance quoted below takes this into account. In the case of strip detectors the load is dominated by the interstrip capacitance and the incomplete charge collection leads to a spreading of the signal over several amplifiers. The expected position resolution is not deteriorated, since the signal spreading can be corrected by a deconvolution algorithm.

The preamplifier output is followed by a resistor which together with the pipeline capacitors forms a low pass filter. Prototype chips have shown a 10–90% signal risetime of 80 ns, which is sufficiently fast for operating at HERA.

The pipeline buffer has 32 switched capacitors for each channel to store the output voltages of the preamplifiers. During data taking the switches IS and SR are closed. The pipeline shift register cyclically connects one storage capacitor for each HERA bunch crossing to the preamplifier output. On the prototypes, the pipeline has been successfully operated at clock frequencies up to 12.5 MHz. In case of a level 1 trigger the pipeline is stopped and the switches SR and IS are opened, which disconnects the preamplifier input from the strip detector. A new feature of the chip architecture is the possibility to read back the charges stored on any of the pipeline capacitors with the preamplifier. This avoids the problem of DC-matching which arises when a separate read amplifier is used which would also increase the total power dissipation.

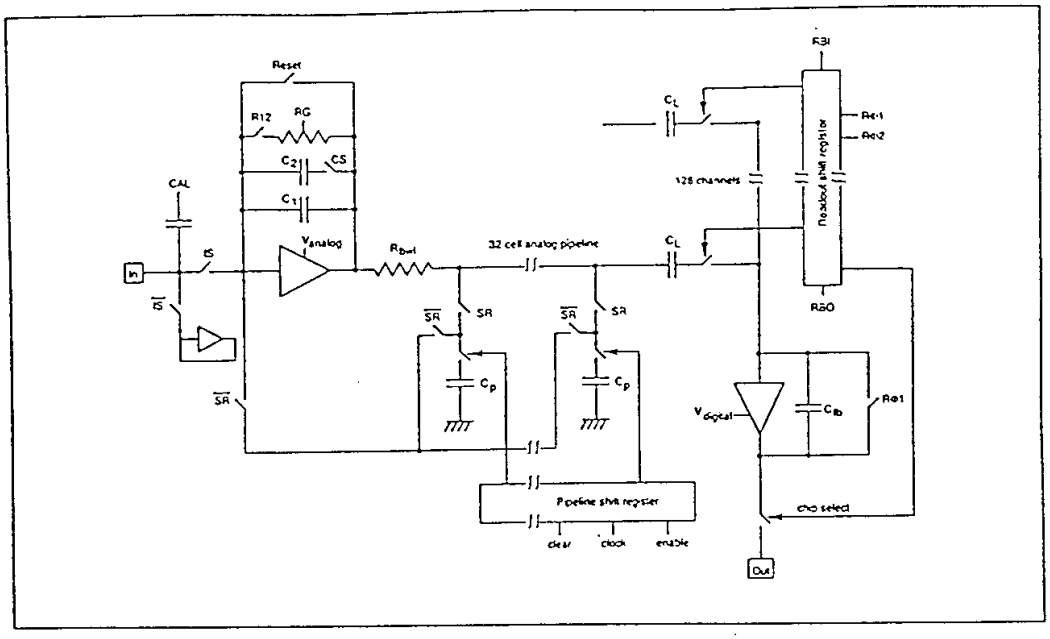

Figure 5.1: *Circuit diagram of the amplifier and pipeline chip (APC).*

The voltage from the pipeline buffer corresponding to the bunch crossing selected by a level 1 trigger, is re-read and stored on the latch capacitor C_L. This has a threefold function. Firstly, it is needed to decouple the DC working points of the preamplifier and the readout amplifier which are operating at different voltages to reduce the over-all power dissipation. Secondly, the latch capacitors are used to perform a pedestal subtraction for all channels in parallel. This is done by resetting the preamplifier and re-reading a buffer from an earlier bunch crossing. Thirdly, the latch capacitors together with the single readout amplifier form another gain stage. A shift register controls the serial readout of the voltages stored on the latch capacitors. Several chips can use the same readout line sequentially. The chip-enable switch ensures, that only one chip at a time is loading the readout line.

With the chip running in its HERA operation mode (10 MHz pipeline, on-chip pedestal subtraction), the equivalent noise charge as a function of the input capacitance has been measured as $680 + 30/\text{pF}$. For the most probable energy loss of minimum ionizing particles in $300\,\mu\text{m}$ of silicon and an input capacitance to ground of 24 pF, a signal-to-noise ratio of 15 : 1 is achieved. The large offset noise of 680 electrons is dominated by the noise from the reset and pipeline switches. The intrinsic preamplifier noise is only about 280 electrons.

The radiation hardness of the CMOS process has been studied. Test structures and prototype chips were irradiated with a Co^{60} source up to a total dose of 240 krad. The usual threshold shifts for MOSFETs have been observed. The circuit design and layout includes two features that allow for a compensation of threshold shifts over some range: constant current power supply and back-gate biasing. Threshold voltage shifts change the operating point of the amplifier. By using a constant current source the preamplifier self-adjusts to the appropriate supply voltage. The APC can be pictured as a multidifferential amplifier system which is operated in a low occupancy environment. Therefore, current biasing is possible. On the prototypes, the amplifiers adjusted

to threshold voltage shifts of up to 1 V after a dose of 240 krad. However, an increase of the power dissipation from 280 μW to 400 μW per channel after 240 krad cannot be avoided. The chips were still functional after a dose of 160 krad, while large internal leakage currents were observed after 240 krad. This phenomenon is still under investigation. It could be caused by n-channel FETs where the threshold voltage was reduced below 0 V. This can be compensated by using a back-gate biasing through the substrate, as was demonstrated with test structures. Besides threshold voltage shifts, MOSFET amplifiers usually show an increased noise after irradiation. The constant noise term for our prototypes did not increase significantly, while the noise slope versus input capacitance had doubled after 80 krad. This is the most severe radiation effect observed and it determines the lifetime of the amplifier chip. All radiation effects have to be regarded as permanent, since only small room temperature annealing effects have been observed after 7 months. Comparing to the expected radiation dose for the silicon tracker at H1 (see chapter 3), we conclude that the CMOS process offers sufficient radiation hardness for a lifetime of 10 years.

5.2 Data Reduction and Control

Readout Organisation

After a level 2 trigger the analog signals from all $2 \cdot 10^5$ channels are read out within 800 μs. This is achieved with 148 readout lines. A repeater placed near the end flange of the central chambers contains drivers for the signal lines. Cables are routed via the cable distribution area (CDA) to the electronics trailer where the readout control and trigger modules are installed, see figure 5.2.

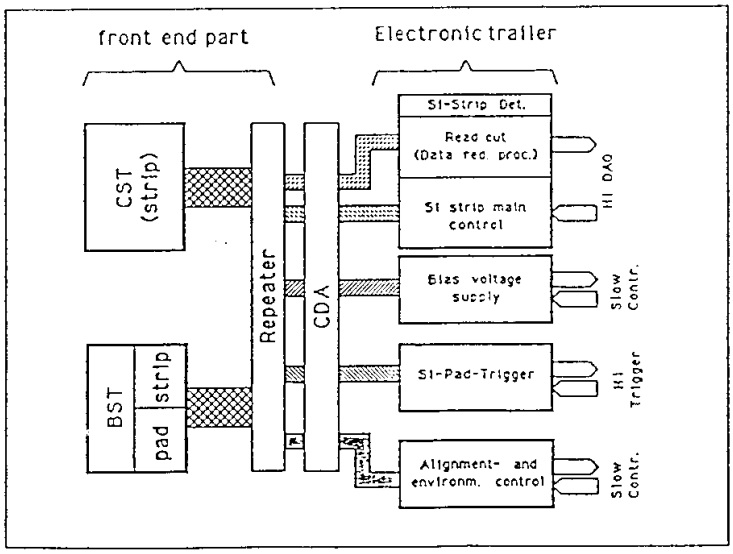

Figure 5.2: *Sketch of the readout organisation.*

Data Reduction and Control

We propose to develop a readout processor which is adapted to the requirements of the H1 data acquisition system.

On the incoming data an analog pedestal subtraction is performed. For each channel and each pipeline buffer a pedestal value is stored in RAM. The data are digitized by 12 bit FADCs, running at sampling frequencies up to 10 MHz, and passed to a programmable hit detector. Since signals from inclined tracks spread over several strips a cluster analysis is used which discriminates on the summed pulseheights from adjacent channels. The hit detector reduces the data size from initially 2.5 Mbit to about 3 kByte.

Figure 5.3 shows a block diagram of the on-line silicon readout and control unit (OnSiRoC). On a standard VME board it contains:

- four data lines for the sequential readout of up to 4 × 2048 silicon strips,
- electronics for the digital controls of the APC,
- digital and analog power supplies for the chips and the detector bias voltage,
- interfaces to the VME bus and the H1 Subdetector Trigger Controller,
- electronics to test the APC.

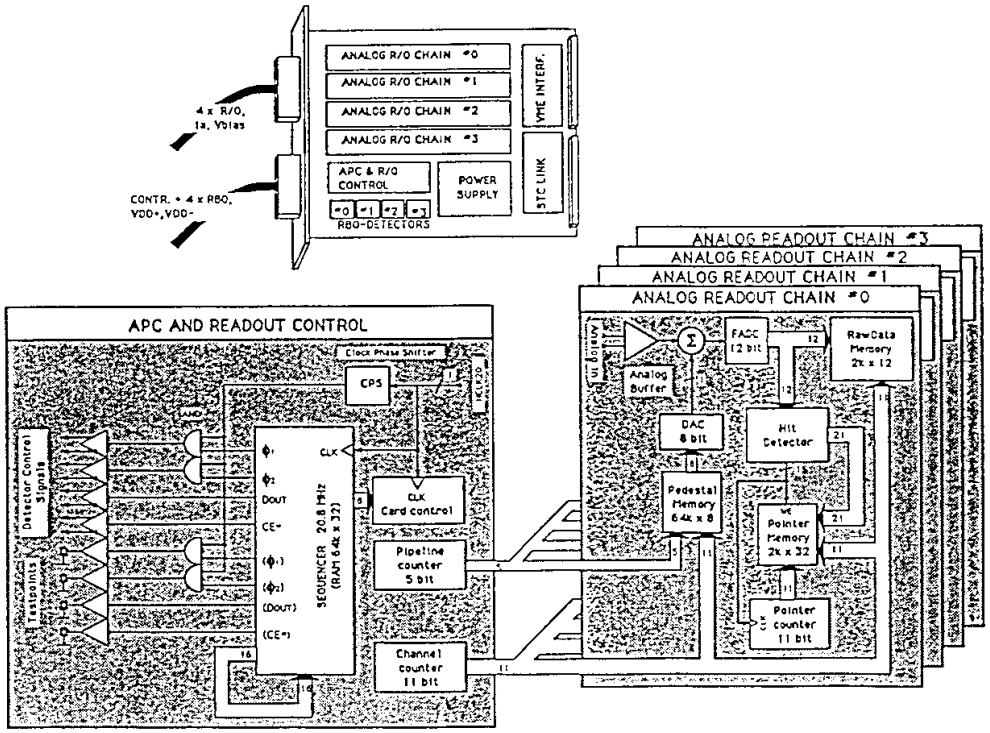

Figure 5.3: *Block diagram of the silicon strip readout and control unit (OnSiRoC). The module has standard VME size (6 height units) and can read out and control up to 4 × 2048 channels.*

After a trigger decision to keep the event, the identified hits are read out from the OnSiRoC modules via VME bus and are analysed by a front-end processor (Motorola 68040). The processor also loads data like pedestal values and parameters for the hit-detection algorithm to the OnSiRoC.

Each OnSiRoC module provides digital controls and power supplies for the APC. In order to reduce the number of control lines from 14 to 4, a serial-to-parallel controler chip is being developed which will be placed on the front-end hybrids.

The silicon tracker DAQ system requires 3 OnSiRoC VME crates and one master crate which contains a multi-event buffer. The master crate communicates with the H1 event builder via VME DMA. The silicon detector readout forms a further branch of the H1 data acquisition system [61]. Table 5.1 gives the number of channels to be handled by the DAQ system.

	Strip Detectors			Trigger Pad	
	CST	BST(r)	BST(φ)	BST	Total
channels	66560	98304	49152		214016
lines	52	64	32		148
OnSiRoC units	13	16	8		37
Trigger pads				1024	1024
Trigger modules				32	32

Table 5.1: *Numbers of channels and readout processors.*

5.3 Trigger Electronics

Preamplifiers

A minimum ionizing particle traversing a layer of 380 μm silicon generates about 28 000 electron-hole pairs. The collected charge in the p^+ layer can be read out with charge sensitive or current sensitive amplifiers. Currently we are testing available VLSI chips of both types (namely the 'VIKING' [62] and the 'ICON' [63]). Both amplifiers have a gain of about 50 mV/fC and a shaping time of 45 ns. One chip comprises four channels.

The readout amplifier is followed by a discriminator. Figure 5.4 shows a schematic drawing of the pad detector readout circuitry. The discriminator threshold can be adjusted externally to give a negligible rate of triggers due to random electronic noise. The readout chips are glued onto a hybrid, serving as printed circuit board and as mechanical support, and are bonded to the pad detector.

The use of the amplifiers for the pad detectors requires a redesign in view of the high capacitive input loads (up to 60 pF) and of input currents of up to 100 nA, as possibly caused by radiation damage [64]. Moreover, it is planned to include the comparator into the readout chip, because separate comparators increase power consumption and occupy more space on the hybrid.

Trigger Logics

After summing the signals of 4 pads, each BST pad detector provides 8 trigger signals, amounting to a total of 512 signals for BST-1 and 1024 for BST-2. Kapton cables connect the discriminators

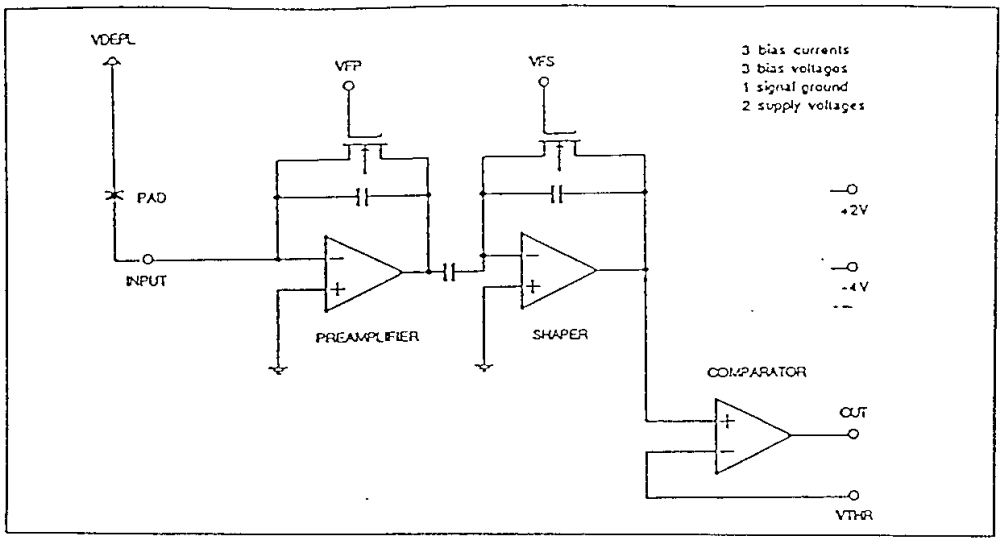

Figure 5.4: *Pad detector readout circuitry.*

on the hybrids to the repeater and twisted pair cables are used for the link to the electronics trailer (see figure 5.5).

The trigger electronics evaluates the hit pattern and determines the hit multiplicity for each bunch crossing. Due to the parallel readout of the signals a decision can be made within $2\,\mu s$ to be conform with trigger level 1. The trigger processing is synchronized to the HERA clock. The discriminator outputs are compared to a number of predefined masks, formed by multiterm logic combinations. With a maximum of about 100 masks (see section 4.5 and [40]) a single configurable logic block of a XILINX 3000 provides enough gates for most of the equations. An electrical erasable memory on each trigger logics card stores the configuration for the arrays.

Each trigger module (figure 5.6) evaluates one φ sector for 4 disks (i.e. 32 signals) independently. It provides a standard 8 bit output [65] of trigger elements identifying the mask pattern to the L2 central trigger logic. Four trigger modules are integrated into a standard VME unit, which also includes power supplies and slow control circuitry. For the BST-1, four VME units are needed. The cards are connected via the auxiliary VME-backplane to a master logic card, where a global *OR* of the independent sector decisions and a summation of the individual multiplicity counts is performed, resulting in a level 1 trigger decision. The master card also contains power supplies and generates control signals. All BST trigger modules fit into one VME crate.

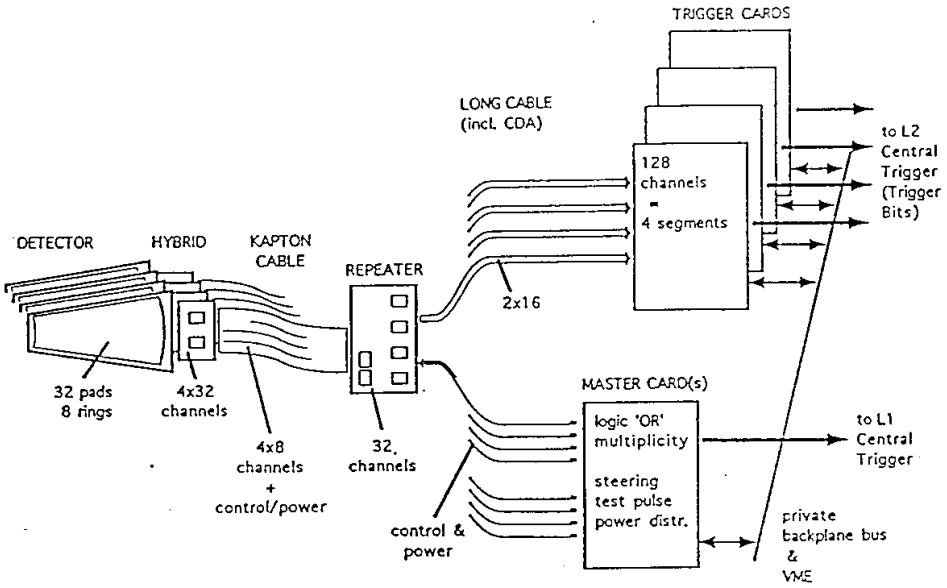

Figure 5.5: *Readout chain for the BST trigger.*

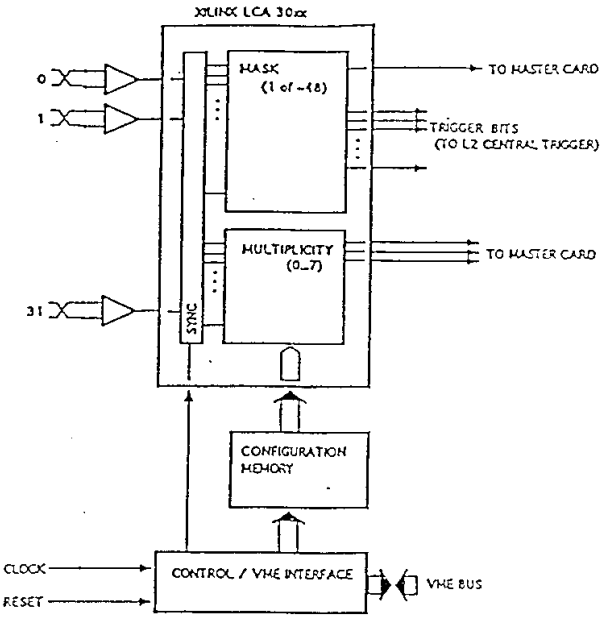

Figure 5.6: *Trigger card. Synchronisation, mask logic and multiplicity calculation for four disks and one φ-sector are implemented in a programmable logic array. The trigger card holds four arrays, a DAQ and VME interface and outputs to the level 2 trigger.*

Chapter 6

Construction and Assembly

6.1 Beampipe

We propose to install a narrow beampipe made from carbon fibre with an aluminium foil on the inside to carry the image current of the beam. For a beam pipe diameter of 70 mm the critical wall thickness is 0.5 mm. A safety factor of three is usually applied although the computed values for buckling agreed with crash tests at CERN within 10%. Nevertheless we propose a wall thickness of 1.5 mm which together with an aluminium foil of 50 μm thickness corresponds to 0.6% of a radiation length.

A problem encountered during the prototype development and also experienced at CERN is the adhesion of the aluminium to the carbon-fibre. A chemical treatment of the aluminium with chromic acid to remove the oxide layer is necessary, followed by a sealing process. As an alternative we also study a replacement of the 50 μm aluminium layer by 18 μm of copper.

The narrow beam pipe has a length of about 5 m, extending to $z = -2.8$ m. Due to the required offset of 10 mm, excentric flanges are needed for the connection to the adjacent beam pipe sections. The ion getter pump which is presently installed at $z = -1.8$ m has to be relocated. Finally, the synchrotron radiation collimators C_3, C_4 and C_6 have to be upgraded, while C_5 becomes obsolete (see section 3.3).

6.2 CST

The mechanical structure of the CST has to ensure a position stability of 5 μm, while minimizing the amount of material used. Our design exploits the rigidity of the silicon wafers and uses carbon fibre for all support structures. The full CST including supports and cables weighs less than 1 kg. The small thermal expansion coefficients of carbon fibre and silicon, combined with low power electronics and water cooling, result in a system with good stability. A 3-D mapping determines the location and orientation of each wafer in space and provides starting values for the final software alignment with particle tracks. Each assembly step is complemented by a test procedure in order to identify bad components as early as possible.

Testing of Components

All strip detectors, readout chips and hybrids will be tested in our laboratory. The detector tests verify that the manufacturer reached the device specifications given in section 4.1. They include measurements of the leakage current, depletion voltage, interstrip resistance, coupling capacitors and bias resistors. Measurements on individual strips are made with probe cards and computer controlled instruments. The functionality of the readout chips can be tested before bonding by using a probecard. Hybrids are tested for continuity and insulation.

CST Hybrids

The width of the double sided hybrids for the CST is matched to the full width of a strip detector (about 34 mm). Five readout chips are mounted on each side of a hybrid. There are 2 analog output lines, 3 supply lines and 14 differential digital control lines on each side of the hybrid, and 1 line for the detector bias voltage. The number of lines can be reduced by adding a digital controler chip, which generates the necessary signals from fewer input lines (see section 5.2). Otherwise, the hybrid contains only passive components like filter capacitors and resistors. A short Kapton cable provides the connection to a printed circuit board on the end flange.

Each readout chip dissipates about 40 mW of power, which amounts to 0.4 W per hybrid and 10 W at each end flange. We consider to use hybrids made from beryllia (BeO), which have an 8 times better thermal conductivity than the conventional alumina substrates. The heat is finally removed in a water pipe that is integrated to the end flanges.

The assembly of the double sided hybrids begins with reflow-soldering of surface mount components and of a short Kapton cable. The readout chips are glued to the hybrids on both sides and the supply lines are wire bonded. Special mechanical fixtures are being designed to hold the hybrids in the bond machine. The full functionality of these readout units can be tested with the calibration lines to the preamplifier inputs. It is possible to replace bad chips after glueing and bonding.

CST Ladders

Three detectors and one hybrid are joined to form a ladder by glueing carbon fibre strips along their sides, which results in an I-beam structure with good stability (see figure 6.1). The carbon fibre strips are about 2 mm high and 0.3 mm thick. The detector edges have to be parallel to the strips within 0.1 mrad. This can be achieved by using alignment marks when the detectors are cut from the wafers.

The readout strips are daisy-chained with wire bonds on both sides. There are three bonds per channel, resulting in 3840 bonds per ladder. The bonding will be performed on a semi-automatic bonding station, which has an x-y table driven by a stepping motor with 1 μm resolution and controlled by a computer. An LED is used to scan across the detectors to test the functionality of the readout chain and to identify dead channels.

Two ladders are connected mechanically with a carbon fibre strip to form a 'face'. A face consists of 6 strip detectors with readout hybrids at both ends and has a total length of about 40 cm. The faces are mounted on the end flanges using screwholes in the hybrids. Individual faces can be replaced in cases of failures.

The CST has 52 ladders which contain 156 silicon strip detectors and 520 readout chips for 66 560 channels. The total silicon area is 3130 cm^2 and the silicon mass 220 g.

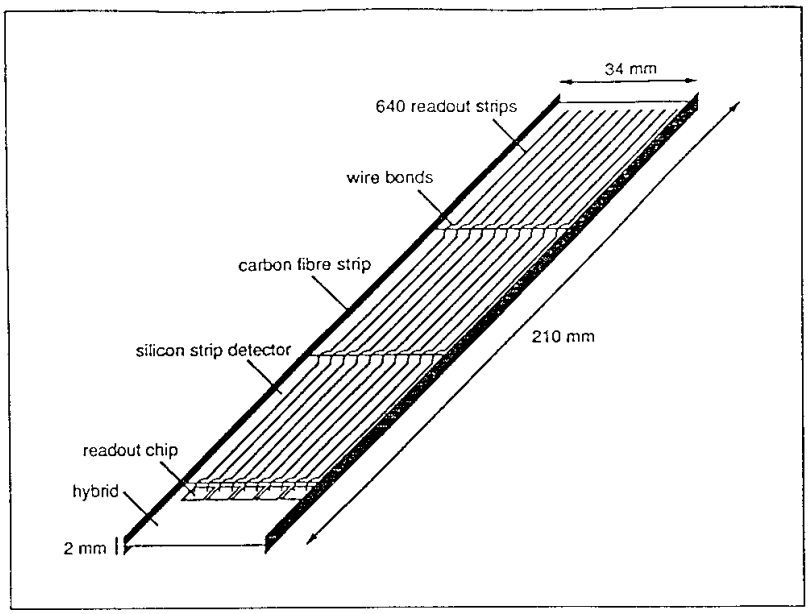

Figure 6.1: *CST ladder.*

CST End Flanges

Each end flange is made of two thin carbon fibre disks separated by 4 mm carbon fibre spacers. One flange weighs about 70 g and represents 0.6 % of a radiation length at normal incidence. The hybrids are attached to carbon fibre supports which contain a water pipe for cooling. The Kapton cables from each hybrid are fed through openings in the end flanges.

During assembly, the end flanges are held in a rotating fixture, which also contains removable rods joining the end flanges. After mounting the inner layer, each wafer position is measured in space to an accuracy of 5–10 μm over a range of 40 cm. The fully assembled CST can be split into two half-cylinders in order to install it around the beam pipe.

A printed circuit board on the end flanges is used to distribute control signals and supply lines to each hybrid. It contains line drivers for the analog signals serving 1.5 m of Kapton cable to the repeater. One option for the digital control signals uses optical fibres for the connection from the electronics trailer to the end flanges where receivers can be placed. This solution reduces the risk of disturbing the adjacent chambers with 10 MHz clock pulses.

CST Shielding and Cabling

The CST is enclosed in a shield made of Rohacell and an aluminium foil. The shield extends around the end flanges to protect the front-end electronics against electromagnetic interference. The shield also provides mechanical protection during installation.

Strip lines from the $+z$-end flange are routed along the shield to the $-z$-end. An adapter tube made of Rohacell is used to guide all CST strip lines with good shielding around the BST to the repeater.

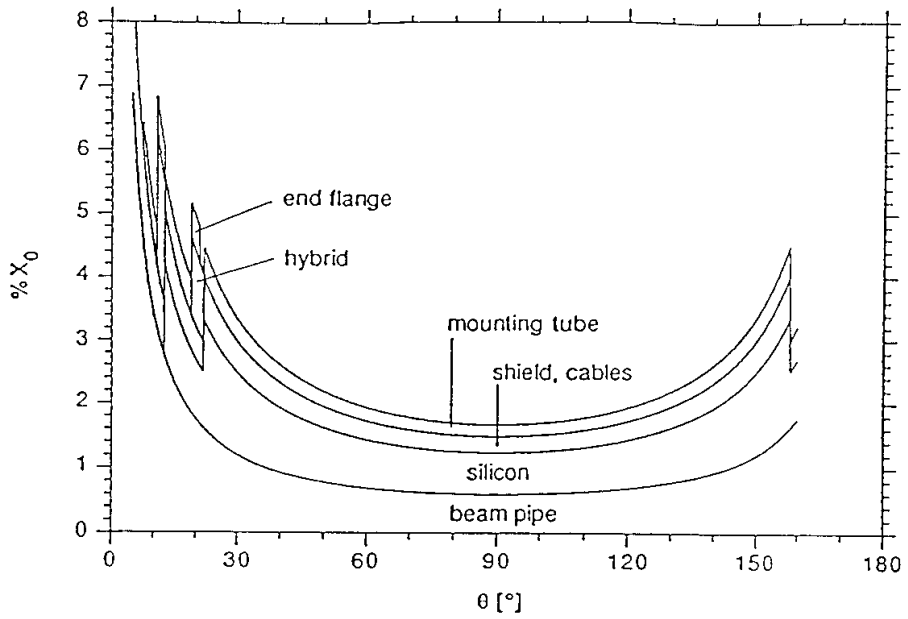

Figure 6.2: *Material thickness of the beam pipe and the CST in percent of a radiation length versus the polar angle.*

Figure 6.2 shows the material contributed by the CST as a function of the polar angle. At $\vartheta = 90°$ the beam pipe contributes 0.6% of a radiation length and the two silicon layers with all cabling and shielding add 1.0%.

Mechanical Support

The silicon tracker is supported by a mounting tube of 150 mm radius, which is attached to the end flanges of the inner MWPC (see section 6.4). The mounting tube contains two carbon fibre rails for insertion and fixation of the silicon detectors. The edge of the lower rail is displaced by 10 mm to center the CST around the off-axis beam pipe. The CST is supported by three carbon fibre legs, as shown in figure 6.3. The end position in z is defined by fixtures glued to the mounting tube. A placement accuracy of 1 mm is sufficient, and the position with respect to the other tracking detectors will be measured to an accuracy of 0.1 mm.

6.3 BST

BST Sectors

The BST is made of disks which consist of layers of silicon detectors: pad detectors, r-strip detectors in phase 1 and additionally φ-strip detectors in phase 2. The smallest mechanical substructure is a φ-sector with one or two silicon detectors and one multilayer hybrid. The strip detectors hybrid is double sided and is connected on one side to the r-strip detector and on the other side to the φ-strip detector. The limited radial space requires the hybrids to be split into

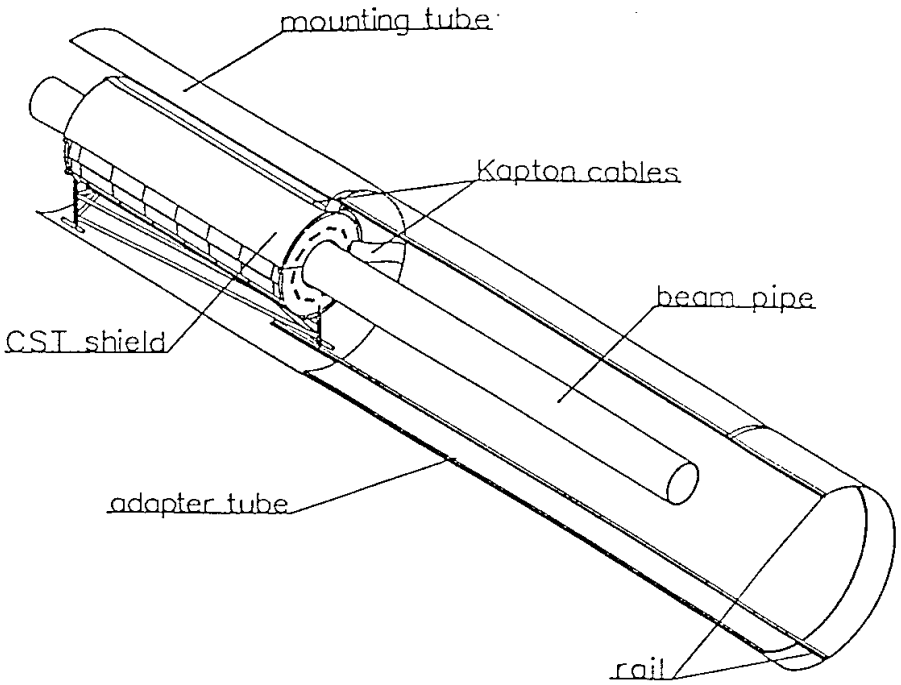

Figure 6.3: *Placement of the CST in the mounting tube.*

a radial and an axial section (r-hybrid and z-hybrid, see figure 6.5).

Surface mounted passive components and a connector are soldered to the hybrid. Readout chips are then glued and bonded to it. The assembled hybrid will undergo a functionality test in a special test adapter. Detectors are glued to the hybrids. The glueing needs a special tool, allowing x, y and φ fine adjustment referencing three cross-hair markers on the detector to two mounting holes in the hybrid. Finally the detectors are bonded to the inputs of the readout chips. The pad detectors may be bonded manually. The large number of bonds per strip detector requires a semi-automated procedure on the basis of a motorized chuck displacement with an integrated test against shorts of the AC coupling oxide. Assembled sectors undergo a laser diode scan to record the performance of every strip.

BST Assembly

After the sectors are tested, they are mounted to a flat 'half wheel' with 5 spokes made entirely from carbon fibre reinforced epoxy (CFRP) (cf. figure 6.4). It has precision machined surfaces for the fixation of the hybrids. Adjacent hybrids are staggered in z to allow for about 3 mm effective overlapping in φ. The hybrids are fixed at the outer ring of the wheel by two screws, one fixed, the other one allowing concentric adjustment of the detector with respect to the wheel axis. The adjustment procedure is supported by computer aided measurement techniques. The inner ring of the half wheel carries slots for the z guidance of the detectors, no further r or φ fixation is provided here (see figure 6.5). The relative positions of the detectors on every half disk are measured.

The completed disks are joined by means of CFRP rods (see figure 6.6). The rods with a diameter of 4 mm extend over the full z range of the BST and provide the necessary stability.

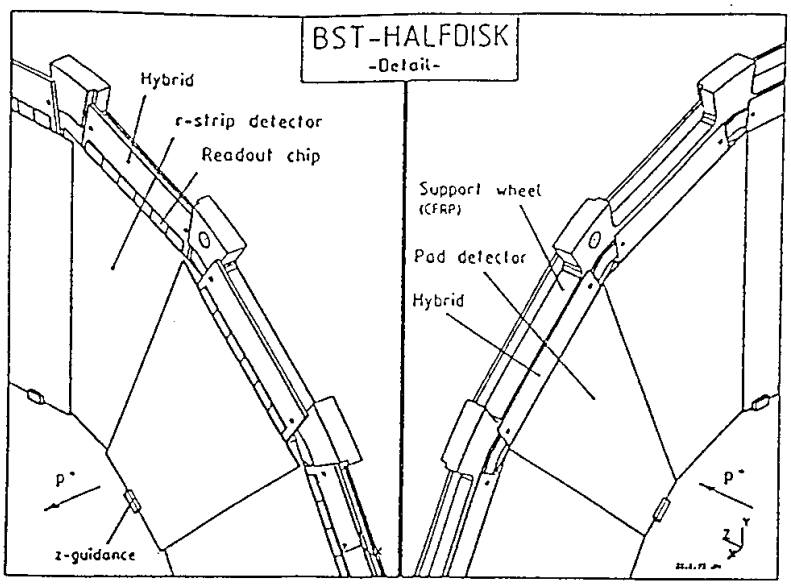

Figure 6.4: *View on a half disk of the BST carrying 8 pad and 8 r and φ strip detectors. Also shown are the respective hybrids with readout chips glued to them. Note the staggering between adjacent detectors.*

Sleeves with a wall thickness of 0.5 mm slide over the rods to define the z position of the disks.

The cables for the BST are plugged into sub-miniature connectors of 0.5 mm pitch on the hybrids. Line drivers are placed on the z-hybrid (figure 6.5). The z-hybrids of 8 sectors (half a disk) are linked to form a 'φ bus'. This bus allows a local distribution of digital control signals in order to reduce the number of interconnects.

In phase 1, the BST strip detectors have 49 152 readout channels which requires 32 readout lines for 2 MHz ACP readout rate. The BST-1 trigger requires 512 lines.

With a power consumption of 40 mW per APC chip, the r-strip and φ-strip detectors dissipate $\approx$ 6 W per disk while the pad detector electronics dissipates $\approx$ 1 W per disk. Altogether this yields about 60 W for the fully equipped BST and about 20 W for BST-1. This can be absorbed by a water cooling system as shown in figure 6.7.

The BST is composed of two symmetric half shells. The halves are enclosed by an inner and outer Faraday cage (1 mm Rohacell and 0.5 mm CFRP, both coated with 50 μm Al). They are joined by matching dowel pins around the beam pipe.

The BST slides into the mounting tube of the silicon tracker guided by a V-shaped ball race at the bottom ($\varphi = 270°$) and a T-shaped rail at top position ($\varphi = 90°$) which are laminated to the mounting tube during manufacturing, see figure 6.8. A specially constructed assembly tool is necessary to provide support for the BST upon roll-in. A 3D-visualization of the BST is shown in figure 6.9.

Figure 6.10 shows the material distribution of BST-1. The main contributions to the material in front of the inner tracking chambers arise from the beam pipe and from the BST cables (both contributing about 5% of X_o at $\vartheta = 170°$). Since the silicon disks are nearly perpendicular to the crossing tracks it was decided to install single sided (pad and r-strip) detectors in the BST-1. With BST-2, where each disk consists of three silicon detectors, we want to measure low hadron momenta. In this context it is suggested to combine r-strip and pad detectors to one double

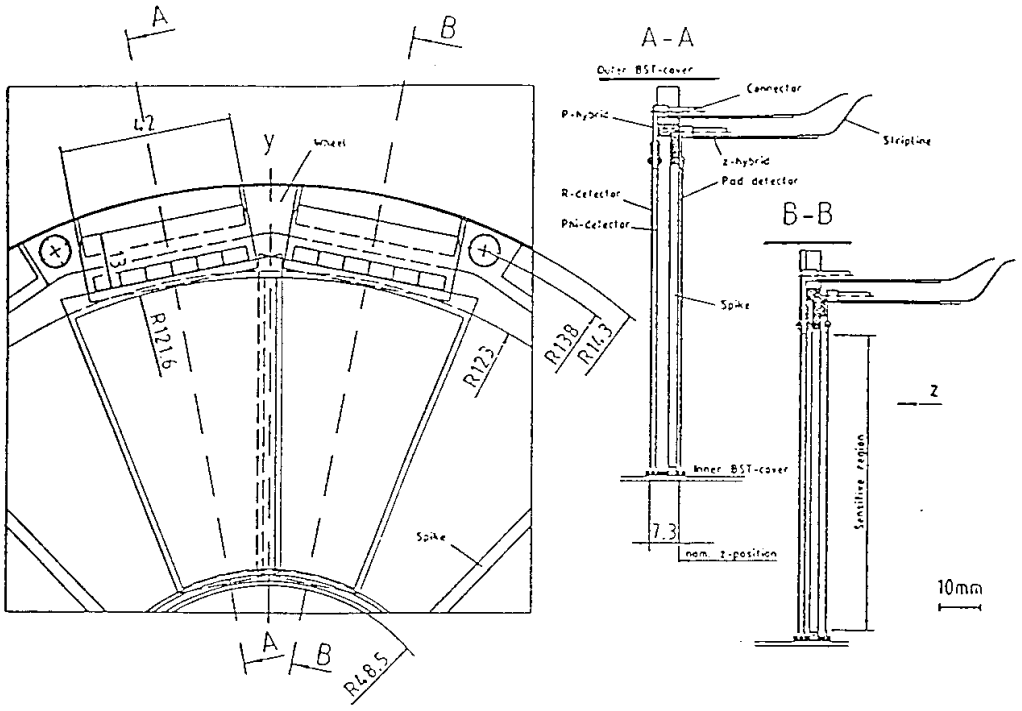

Figure 6.5: *BST disk - details and section. Left: details and dimensioning of the support wheel; right: sections showing the three detectors, the hybrids and the stripline connectors.*

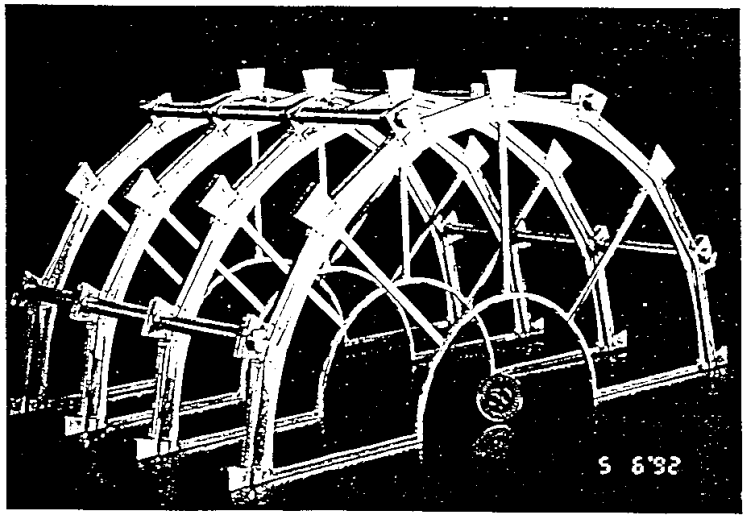

Figure 6.6: *Mechanical support structure of BST-1 in a 1:1 model made of aluminium.*

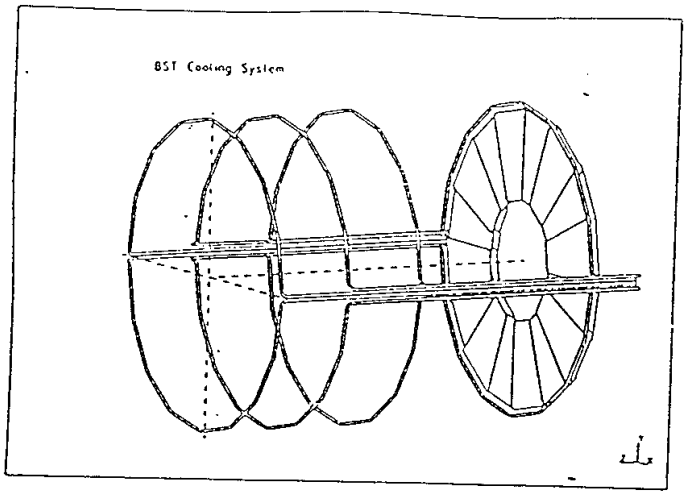

Figure 6.7: *Water cooling system for BST-1. Each half disk has its own pipe ($2 \times 0.2\,mm$ Al), which is conneced to the heat emitting hybrids by a flexible foil of* $0.4\,mm$ *Al.*

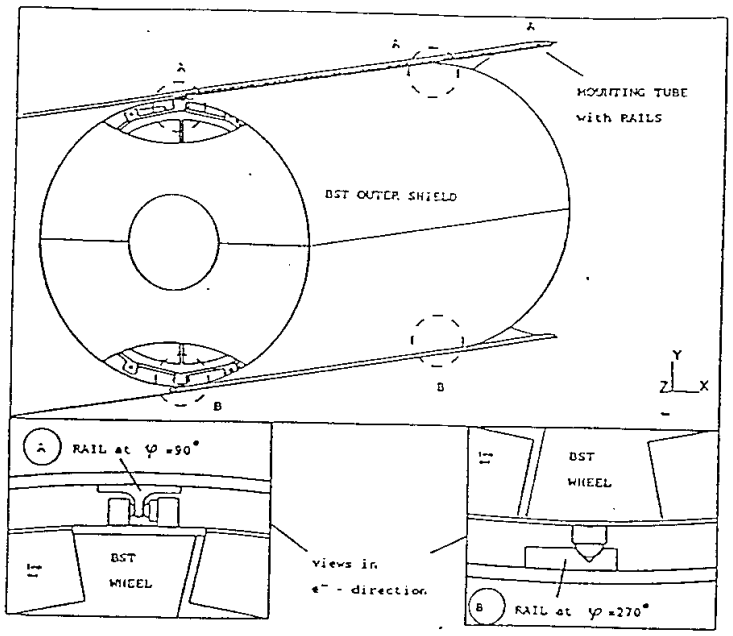

Figure 6.8: *Details of the BST guidance in the mounting tube. The BST slides on a V-shaped rail at bottom while guided by a T-shaped rail at top. The asymmetric edge of the bottom rail defines the off-beam position of the CST.*

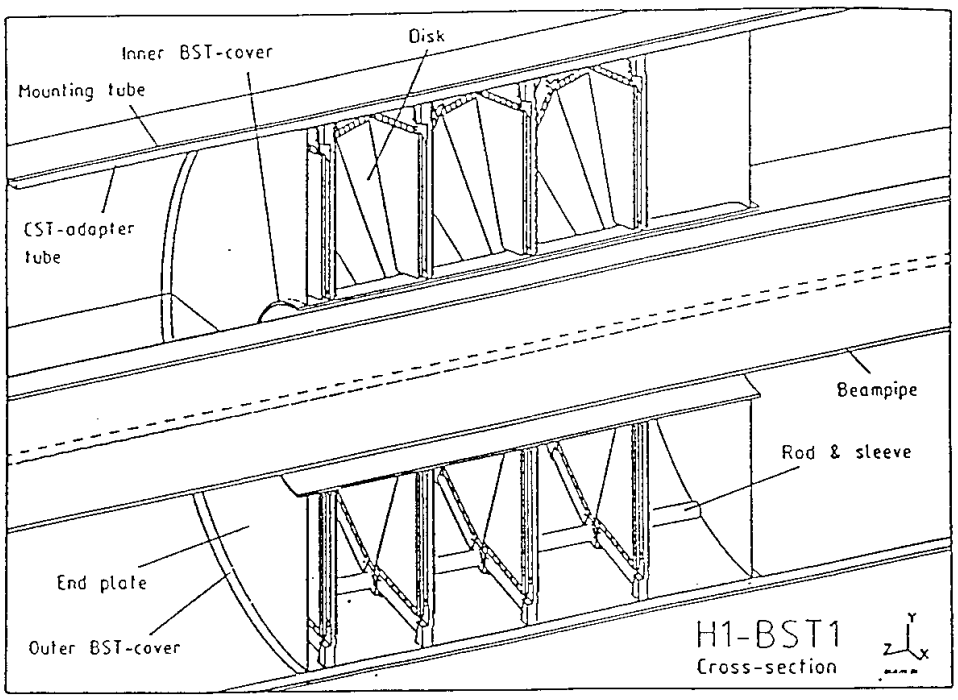

Figure 6.9: *3D view of a BST-1 half.*

sided silicon detector [47].

Alignment of the BST

The alignment of the BST requires to adjust 8 detectors concentrically on the frame of a half disk. Optical measurements on an x-y table allow to keep the tolerances at the level of $10\,\mu m$. The BST disks will be optically aligned, the BST assembled and the relative r and z positions of each disk be measured. Radial displacements beyond the required accuracy can be recognized from the data utilizing the φ overlap of adjacent detectors and the huge statistics of straight tracks at low Q^2. For the required polar angle resolution the z positions have to be known within $100\ \mu m$. The distance between adjacent disks is defined to better than $100\ \mu m$ with the thin sleeves between them. If necessary, coordinate measurements of the assembled two half shells can be realized on a 3D measurement device because the detector halves are open towards the beam pipe before the Faraday cage will be closed.

The two half shells are positioned with respect to each other in z by dowel pins. If the central axis of the BST is off the beam line, this can be recognized by comparing the polar angles measured with and without the vertex determined by the central detector chambers. Tilts of the BST axis against the beam line can be kept below 1 mrad. Below $\vartheta = 170°$ the overlap with the inner z drift chamber (CIZ) allows a cross calibration of the two detectors.

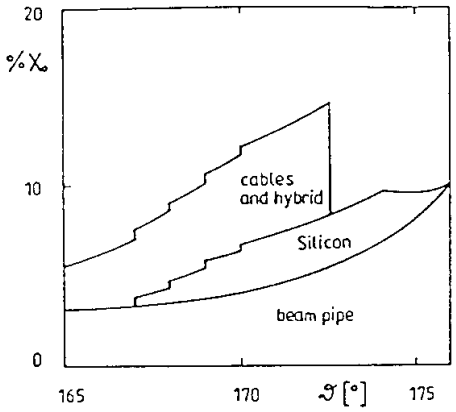

Figure 6.10: *Material distribution of the BST in percent of a radiation length versus the polar angle.*

6.4 Common Infrastructure

Mounting Tube

The silicon trackers are installed in a mounting tube, made of carbon fibre with 297 mm diameter and 2467 mm length and attached to the end flanges of the inner MWPC and inner z-drift chamber. The wall thickness is 0.5 mm, corresponding to 0.2% of a radiation length.

Two carbon fibre rails, at $\varphi = 270°$ and $90°$ are used to guide the CST and BST when the silicon tracker is inserted from the $-z$-end and to fix the CST and BST positions in the φ-direction. The rails (figure 6.8) are integrated to the tube during processing in order to ensure their straightness.

The end positions in z are determined by carbon fibre stops that are glued to the inside of the mounting pipe.

Repeater and Cables

The repeater receives Kapton cables from the detectors and interconnects to about 40 m of coaxial cables to the electronics trailer. It provides line drivers for the analog readout lines.

The cables are routed from the repeater to the trailer via the Cable Distribution Area (CDA) at the flange of the H1 liquid argon cryostat, where space for the cables of a vertex detector was allocated in the design.

Sixteen OnSiRoC modules fill a crate and three crates are needed for the strip detectors of the CST and the BST. For the master crate, the subdetector trigger controller and the BST trigger three further crates are needed. Thus a rack space for 6 standard VME crates is requested for the silicon tracking detectors. These can be placed in two racks at the lower level of the electronics trailer.

6.5 Installation Procedure

The installation of the silicon tracking detectors is performed in three steps:

1. Installation of the mounting tube inside the CIP and CIZ,
2. Installation of the new beam pipe,
3. Installation of the CST and the BST.

The first and second steps are only possible, if the H1 detector is in the 'garage position' outside the interaction area. It is not necessary to remove the tracking detectors. The installation of the mounting tube can be performed with tools used already to remove the CIZ in situ. The installation of the beam pipe can also be performed using existing tools. The half shells of the detectors are joined around the beam pipe. A special tool extends the rails of the mounting tube and allows the detectors to be slid to their final position.

Experience with existing silicon detectors shows, that it is necessary to have annual access to the detectors. At present, the BEMC can be removed while H1 is in beam position. For the future backward calorimeter we request to have access to the silicon tracker. In order to introduce the mounting tube extension (diameter $\approx$ 400mm) and to get a lateral access of $\Delta z \approx 800\,\mathrm{mm}$, a central part or the complete future backward calorimeter must be removable.

The BST can be removed without uncabling the CST. The cabling from the repeater to the CDA requires access to the $-z$-endwall of the CTD. The routing of the cables from the CDA to racks B8 and B9 in the lower level of the trailer may require some repositioning of existing cables. It may be necessary to install all cables for the BST at once, including those for BST-2.

Chapter 7

Finances, Responsibilities and Schedule

The responsibilities to build the silicon trackers are shared in general as follows: the Swiss groups are responsible for the CST and both DESY groups are responsible for the BST. The major parts are developed and built under the reponsibility of the following institutes:

CST	(complete detector)	ETH, Uni. Zürich, PSI
BST	(r-detectors, mechanics)	DESY Zeuthen
BST	(φ-detectors)	DESY Hamburg
APC readout chip	(for CST and BST)	PSI
readout processor	(for CST and BST)	DESY Hamburg
BST trigger	(pad detectors, electronics)	DESY Zeuthen
Beam pipe	(central part)	ETH
Infrastructure	(vacuum system, general tools)	DESY Hamburg

A break down of the necessary investments is shown in table 7.1. Costs for technical manpower in the institutes, for prototyping and for contingency are not included.

We plan to install the CST and the BST-1 during a shutdown early 1994, the remaining parts of BST-2 will be added when the new backward calorimeter will be installed. It is assumed that BST-2 is ready for installation early 1995. In table 7.2 the funding profile to finance the silicon tracker is given. The time planning requires that milestones are met, as listed in table 7.3, for each of the major components.

Item	CST (Swiss Institutes)	BST (DESY)	
		phase 1	phase 1+2
	(kDM)	(kDM)	(kDM)
Detectors	600	450	1200
APC readout chip	120		
Trigger front-end		50	80
Hybrids	10	10	30
Detector mechanics	100	50	150
Readout processors	180	100	300
Trigger electronics		90	140
Cables	50	100	100
Implement. into H1 DAQ		80	120
Beampipe	50	100	100
General mechanics	50	100	100
SUM	1160	1130	2320

Table 7.1: *Project investments. Prices for BST-1 are included in BST-2. Numbers are given based on estimates and quotations of spring 1992.*

	1992	**1993**	1994	**1995**
Swiss Institutes	10%	50%	40%	
DESY		50%	30%	20%

Table 7.2: *Funding profile for financing the silicon tracking detectors.*

Component	end of prototype development	end of series production
CST detectors	I/93	IV/93
BST-1 detectors	I/93	IV/93
BST-2 detectors	IV/93	III/94
APC readout chip	IV/92	II/93
Data reduction processor	III/93	I/94
Trigger electronics	II/93	IV/93
Beampipe (narrow part)	I/93	II/93

Table 7.3: *Milestones for building the major components of the silicon trackers.*

Bibliography

[1] J. Bürger *et al.*, H1 internal note, H1-03/91-164, March 1991;

[2] H1 Collaboration: *Technical Proposal* DESY internal rep., PRC-86/02 (1986):

[3] C. Adolphsen *et al.*, Nucl. Instr. and Meth. A313 (1992) 63;

[4] W.C. Carithers *et al.*, Nucl. Instr. and Meth. A289 (1990) 388;

[5] R. Eichler, Z. Kunszt, Nucl. Phys. B308 (1988) 791;

[6] R.K. Ellis and P. Nason, Nucl. Phys. B312 (1989) 551;

[7] J.C. Anjos *et al.*, Phys. Rev. Lett. 65 (1990) 2503;

[8] M. Wielers, Diploma Thesis, RWTH Aachen, PITHA 92/1 (1991);

[9] R. v. Woudenberg et al., DESY report, DESY 92-002 (1992) and Proc. Intern. Workshop "Physics at HERA", Hamburg 1991, DESY, in press;

[10] F. Ould-Saada *et al.*, DESY report, DESY 91-138 (1991) and Proc. 4^{th} Int. Symp. Heavy Flavour Physics, Orsay 1991;

[11] L. Wolfenstein, Phys. Lett. B164 (1985) 170;

[12] L.L. Chau, Phys. Rep. 95 (1983) 1;

[13] J.C. Anjos *et al.*, Phys. Rev. Lett. 60 (1988) 1239;

[14] S. Egli, C. Grab, F. Ould-Saada, H. Simma and D. Wyler, ETH preprint, ETHZ-IMP PR/92-1 (1992) and Proc. Intern. Workshop "Physics at HERA", Hamburg 1991, DESY, in press;

[15] S. Pakvasa, S.F. Truan, S.P. Rosen, Phys. Rev. D42 (1990) 3746,
M. Savage, R. Springer, Phys. Rev. D42 (1990) 1527;

[16] A.N. Aleev *et al.*, Sov. J. Nucl. Phys. 43 (1986) 395;

[17] M. Jezabek, K. Rybicki and R. Rylko , submitted to Phys. Lett. B;

[18] P. Avery *et al.*, Phys. Rev. Lett. 65 (1990) 2842;

[19] H. Albrecht *et al.*, DESY report, DESY 91-091 (1991);

[20] J.C. Anjos *et al.*, Phys. Rev. D37 (1988) 2391;

[21] P. Burchat, C. James private communications;

[22] S. Egli, Proc. 3^{rd} Topical Conference on Heavy Flavours, San Miniato 1991;

[23] R. Luchsinger, Diploma Thesis, ETH Zürich 1991;

[24] H. Hanai *et al.*, KEK preprint, KEK 91-175 (1991),
M. Brogle, Diploma Thesis, Universität Zürich, 1992;

[25] R. Feynman, Acta Phys. Pol. 24 (1963) 697 and Phys. Rev. Lett. 23 (1969) 1415,
J. Bjorken and E.A. Paschos, Phys. Rev. 185 (1969) 1975;

[26] EMC collaboration, J. Aubert *et al.*, Nucl.Phys.B293 (1987) 740,
BCDMS collaboration, A.C. Benvenuti *et al.*, Phys. Lett. 223B (1989) 485 and Phys. Lett. 237B (1990) 592,
a compilation and reanalysis of the SLAC data has been presented by L. Whitlow, Ph.D.thesis, SLAC-report 357(1990),
for a compilation of all structure function data obtained see: R.G. Roberts and M.R. Whalley, J. Phys. G. Nucl. Part. Phys.17 (1991) D1;

[27] L.V. Gribov, E.M. Levin and M.G. Ryskin, Nucl. Phys. B188 (1981) 555 and Phys. Rep. 100 (1983);

[28] V.N. Gribov and L.N. Lipatov, Sov. J. Nucl. Phys. 15 (1972) 438 and 675,
G. Altarelli and G. Parisi, Nucl.Phys. 126 (1977) 297,
Yu.L. Dokshitzer, Sov. Phys. JETP 46 (1977) 641;

[29] A. DeRoeck and M. Klein, Proc.Int. Conf. on Hadron Structure, Stara Lesna 1991, Phys. and Applications, Vol.16, Bratislava (1991);

[30] E.A. Kuraev, L.N. Lipatov and V.S. Fadin, Phys.Lett. 60B (1975) 50 and Zh. Eksperiment. I. Teor. Fiz. 72 (1977) 377;

[31] J. Kwiecinski, A.D. Martin, W.J. Stirling and R.G. Roberts, Phys. Rev. D42 (1990) 3645;

[32] J. Bartels, J. Blümlein and G.A. Schuler, Z. Phys. C50 (1991) 91;

[33] A.H. Mueller, Nucl. Phys. B (Proc.Suppl.) 18C (1990) 125;

[34] NMC collaboration, I.G.Bird et al., Proceedings of the Lepton-Photon Conference, Geneva 1991;

[35] M.Klein, Proc. Intern. Workshop "Physics at HERA", Hamburg 1991, DESY, in press;

[36] J. Blümlein, M. Klein and T. Naumann, Proc. 'New theories in physics', Kazimierz, Poland, Singapore (1989), 228,
J. Blümlein and M. Klein, DESY-Zeuthen preprint 92-038(1992) and Proc. Intern. Workshop "Physics at HERA", Hamburg 1991, DESY, in press;

[37] A. Martin, R. Roberts and W.Stirling, RAL preprint, RAL-87-052 (1987);

[38] A detailed account on the photoproduction physics can be found in Proc. Intern. Workshop "Physics at HERA", Hamburg 1991, DESY, in press;

[39] A. DeRoeck and E. Evrard, Brussels 1992, H1-Note 02/92-215;

[40] H. Henschel *et al.*, H1 internal note, H1 04/92-221 (April 1992);

[41] A. Cooper *et al.*, Proc. Intern. Workshop "Physics at HERA", Hamburg 1991, DESY, in press;

[42] C. Callan and D. Gross, Phys. Rev. Lett. 22 (1969) 156;

[43] J. Feltesse, Proceedings of the Workshop on the Physics at HERA, DESY, Hamburg, Vol. 1 (1987), 33;

[44] M. Klein, Proc. 4th Topical Seminar, San Miniato, 1990, Singapore (1991), 31,
J. Blümlein and M. Klein, Proc. Snowmass Workshop "The Physics of the Next Decade", August 1990, in press;

[45] G. Bernardi and W. Hildesheimer, Proc. Intern. Workshop "Physics at HERA", Hamburg 1991, DESY, in press;

[46] N.Wulff, H1 internal Note, H1-06/227-1992, under preparation

[47] B.S. Avset, SI Senter for Industrieforskning, Oslo, Norway, private communication;

[48] T. Kurca, private communication;

[49] J. Morfin and Wu-Ki-Tung, Fermilab preprint, Fermilab-Pub 90/74 (1990);

[50] T.Günzel et al., Heidelberg preprint, HD-PHY/91-XX(1991);

[51] D. Pitzl *et al.*, Nucl. Phys. B (Proc. Suppl.) 23A (1991) 340,
H. Ziock *et al.*, IEEE Trans. Nucl. Sci. NS-38 (1991) 269;

[52] G. Hall, private communication;

[53] S. Khan, private communication;

[54] G. v.Holtey, CERN, private communication;

[55] SI Senter for Industrieforskning, Oslo, Norway,
Hamamatsu Photonics, Hamamatsu City, Japan,
CSEM Centre Suisse d'Electronique et de Microtechnique, Neuchâtel, Switzerland;

[56] H. Ikeda *et al.*, Nucl. Instr. and Meth. A313 (1992) 31;

[57] B.S. Avset, L. Evenson, A. Hanneborg and M. Nese, Proc. Conference on Semiconductor Detectors, Milano, 1992, to be published in Nucl. Instr. and Meth. A;

[58] R. Horisberger, D. Pitzl, Proc. Conference on Semiconductor Detectors, Milano, 1992, to be published in Nucl. Instr. and Meth. A;

[59] SACMOS 2 process from FASELEC, Zürich;

[60] J. Bürger *et al.*, Nucl. Instr. and Meth. A279 (1989) 217;

[61] W.J. Haynes, RAL internal note, RAL-90-039 (1990);

[62] E.Nygård et al., Proc. Conference on Semiconductor Detectors, Milano, 1992, to be published in Nucl. Instr. and Meth. A;

[63] F.Anghinolfi et al., CERN internal note, CERN/ECP 91-25 (1991);

[64] C.Coldewey, DESY internal report, DESY F35-91-02 (April 91);

[65] H. Krehbiel, H1 internal note, H1 trigger note Nr.12, (July 1989).

List of Figures